

Mapping the human subcortical auditory system using histology, post mortem MRI and in vivo MRI at 7T

Kevin Richard Sitek^{1,2†}, Omer Faruk Gulban^{3†}, Evan Calabrese^{4§}, G. Allan Johnson⁴, Agustin Lage-Castellanos³, Michelle Moerel^{3,5}, Satrajit S. Ghosh^{1,2‡}, Federico De Martino^{3,6‡}

***For correspondence:**

orcid.org/0000-0001-7761-3727 (OFG);
orcid.org/0000-0002-2172-5786 (KRS)

[†]These authors contributed equally to this work

[‡]These authors also contributed equally to this work

Present address: [§]Department of Radiology, University of California, San Francisco, USA

¹MIT; ²Harvard University; ³Department of Cognitive Neuroscience, Faculty of Psychology and Neuroscience, Maastricht University, The Netherlands; ⁴Duke University; ⁵Maastricht Centre for Systems Biology, Faculty of Science and Engineering, Maastricht University, The Netherlands; ⁶Center for Magnetic Resonance Research, University of Minnesota, Minneapolis, USA

Abstract Studying the human subcortical auditory system non-invasively is challenging due to its small, densely packed structures deep within the brain. Additionally, the elaborate three-dimensional (3-D) structure of the system can be difficult to understand based on currently available 2-D schematics and animal models. We addressed these issues using a combination of histological data, post mortem magnetic resonance imaging (MRI), and in vivo MRI at 7 Tesla. We created anatomical atlases based on state-of-the-art human histology (BigBrain) and post mortem MRI (50 μ m). We measured functional MRI (fMRI) responses to natural sounds and demonstrate that the functional localization of subcortical structures is reliable within individual participants who were scanned in two different experiments. Further, a group functional atlas derived from the functional data locates these structures with a median distance below 2mm. Using diffusion MRI tractography, we revealed structural connectivity maps of the human subcortical auditory pathway both in vivo (1050 μ m isotropic resolution) and post mortem (200 μ m isotropic resolution). This work captures current MRI capabilities for investigating the human subcortical auditory system, describes challenges that remain, and contributes novel, openly available data, atlases, and tools for researching the human auditory system.

Introduction

Understanding the structure of the human subcortical auditory pathway is a necessary step to research its role in hearing, speech communication, and music. However, due to methodological issues in human research, most of our understanding of the subcortical (thalamic, midbrain, and brainstem) auditory pathway arises from research conducted in animal models. This might be problematic because, while the organization of the auditory pathway is largely conserved across mammalian species (*Malmierca and Hackett, 2010; Schofield, 2010*), the form and function of each structure may not be analogous (*Moore, 1987*). In this paper we show that three human imaging modalities -histology, post mortem magnetic resonance imaging (MRI), and in vivo MRI at ultra high-field (7 Tesla)- can identify the structures of the subcortical auditory pathway at high spatial resolution (between 50 and 1100 μ m).

Although MRI has become increasingly powerful at imaging deep brain structures, anatomical

41 investigation of the human subcortical auditory pathway has been primarily conducted in post
 42 mortem tissue dissection and staining. **Moore (1987)** stained both myelin and the cell bodies of
 43 subcortical auditory structures in four post mortem human brainstem samples and compared them
 44 to the analogous structures in cats (a common model for auditory investigations at the time). Later
 45 investigations from the same group (**Moore et al., 1995**) used myelin and Nissl cell body staining to
 46 investigate the timeline of myelination in human auditory brainstem development. More recently,
 47 **Kulesza (2007)** stained six human brainstems for Nissl substance, focusing on the superior olivary
 48 complex, finding evidence of a substructure (the medial nucleus of the trapezoid body) whose
 49 existence in the human auditory system has been debated for decades.

50 Advances in post mortem human MRI allow for investigating three-dimensional (3-D) brain
 51 anatomy with increasingly high resolution (100 μm and below). This points to "magnetic resonance
 52 histology" (**Johnson et al., 1993**) as a promising avenue for identifying the small, deep subcortical
 53 auditory structures. However, to the best of our knowledge, post mortem MRI has not been utilized
 54 within the subcortical auditory system, although it has provided useful information about laminar
 55 structure in the auditory cortex (**Wallace et al., 2016**).

56 To study the subcortical auditory system in living humans, MRI is the best available tool due to
 57 its high spatial resolution. Anatomical in vivo MRI investigations of the human subcortical auditory
 58 pathway so far have focused on thalamic nuclei (**Devlin et al., 2006; Moerel et al., 2015**), and the
 59 identification of the acoustic radiations between the auditory cortex and medial geniculate nucleus
 60 of the thalamus with diffusion-weighted MRI tractography (**Devlin et al., 2006; Behrens et al., 2007;**
 61 **Javad et al., 2014; Maffei et al., 2018**). The inferior colliculus of the midbrain can also be identified
 62 using anatomical MRI—for instance, **Tourdias et al. (2014)** and **Moerel et al. (2015)** show the inferior
 63 colliculus using short inversion time T1-weighted anatomical MRI at 7 Tesla, although neither
 64 investigation focused on anatomical segmentation of the inferior colliculus. Due to their small
 65 size and deep locations, identification of more caudal subcortical structures—the superior olivary
 66 complex and cochlear nucleus—remain challenging with in vivo anatomical MRI.

67 Although lower spatial resolution than anatomical MRI, functional MRI (fMRI) has been used to
 68 investigate the relevance of subcortical processing of auditory information in humans, but it has
 69 been limited by the small size of the structures involved and the relatively low resolution attainable
 70 at conventional field strengths (3 Tesla and below) (**Guimaraes et al., 1998; Harms and Melcher,**
 71 **2002; Griffiths et al., 2001; Hawley et al., 2005**). These acquisitions required trade-offs, such as low
 72 through-plane resolution (7 mm) in exchange for moderate in-plane resolution (1.6 mm), and in
 73 some cases researchers synchronized image collection to the cardiac cycle in order to overcome
 74 the physiological noise associated with blood pulsation in the brainstem (**Guimaraes et al., 1998;**
 75 **Sigalovsky and Melcher, 2006**).

76 More recent advances in MRI, especially the increased signal-to-noise ratio (SNR) available at
 77 ultra-high magnetic fields (7 Tesla and above), have enabled higher resolution functional imaging of
 78 subcortical structures and more advanced localization of human auditory subcortical structures
 79 as well as their functional characterization. Using MRI at 7 Tesla (7T), **De Martino et al. (2013)** and
 80 **Moerel et al. (2015)** collected relatively high resolution (1.1-1.5 mm isotropic) fMRI with an auditory
 81 paradigm to identify tonotopic gradients in the inferior colliculus and medial geniculate nucleus. In
 82 these studies, high isotropic resolution and SNR provided an opportunity to investigate auditory
 83 responses throughout the subcortical auditory system.

84 Despite the methodological advances in investigating the human brain, a systematic comparison
 85 of their capabilities for imaging the subcortical auditory system has not yet been undertaken. Here
 86 we use publicly available histological data (**Amunts et al., 2013**) to segment the main nuclei along
 87 the subcortical auditory pathway. Using state-of-the-art acquisition and analysis techniques, we
 88 evaluate the ability to identify the same structures through post mortem anatomical MRI, through
 89 functional MRI using natural sounds, and through estimating the connectivity between subcortical
 90 auditory structures with post mortem and in vivo diffusion MRI tractography. To compare the
 91 histological, post mortem, and in vivo data, we project all images to MNI common reference space

92 (Fonov *et al.*, 2009, 2011). Finally, to facilitate dissemination of our results, we have made the post
93 mortem anatomical data, in vivo functional and diffusion data, and the resulting atlases publicly
94 available.

95 Where histology provides ground truth information about neural anatomy, we show that post
96 mortem MRI can provide similarly useful 3-D anatomical information with less risk of tissue damage
97 and warping. We also show that in vivo functional MRI can reliably identify the subcortical auditory
98 structures within individuals, even across experiments. Overall, we found that each methodology
99 successfully localized each of the small structures of the subcortical auditory system, and while
100 known issues in image registration hindered direct comparisons between methodologies, each
101 method provides complementary information about the human auditory pathway.

102 Results

103 Definition of a subcortical auditory atlas from histology

104 To obtain a spatially accurate reference for all the subcortical auditory structures, we manually
105 segmented publicly available histological data (100 μm version of the BigBrain 3-D Volume Data
106 Release 2015 in MNI space from <https://bigbrain.loris.ca> (Amunts *et al.*, 2013)).

107 Upon inspecting this dataset, we noticed that the area around the inferior colliculus was in-
108 correctly transformed into MNI space. This was causing the colliculi to be larger and more caudal
109 than in the MNI reference brain (Figure 7, second and third panels). Thus, our first step was to
110 correctly register the area around the colliculi (Figure 7, fourth panel; see Methods for details on
111 the correction procedure).

112 The results of our BigBrain subcortical auditory segmentation in corrected MNI space are
113 reported in Figure 1 together with schematics redrawn from Moore (1987) (for the cochlear nucleus,
114 superior olivary complex, and inferior colliculus) and the Allen Human Brain Atlas (Hawrylycz *et al.*,
115 2012; Ding *et al.*, 2016) (for the medial geniculate body). These schematics were used as reference
116 during the segmentation. The 3-D rendering of the segmented structures highlighting the complex
117 shape of the cochlear nucleus and superior olivary complex is also presented in Figure 1. The
118 rendering is presented from a posterior lateral view in order to compare it with the Gray's Anatomy,
119 Plate 719 (Gray and Lewis, 1918).

120 Post mortem MRI

121 Post mortem MRI atlas of the human subcortical auditory system

122 Magnetic resonance histology—i.e., the study of tissue at microscopic resolution using MRI—provides
123 several unique advantages over conventional histology: 1) it is non-destructive; 2) it suffers minimal
124 distortion from physical sectioning and dehydration; 3) it yields unique contrast based on water
125 in the tissue and how it is bound (e.g., diffusion); and 4) it produces 3-D data. These advantages
126 make it an ideal medium for visualizing the 3-D organization of the deep brain structures (Johnson
127 *et al.*, 1993). To delineate the subcortical auditory structures with MR histology, we acquired 50 μm
128 isotropic voxel size 3-D gradient echo (GRE) MRI on a human post mortem brainstem and thalamus
129 (described previously in (Calabrese *et al.*, 2015); see Methods for additional details). These data are
130 presented in Figure 2 (second column) after transformation to MNI space and resampling to 100
131 μm isotropic resolution (see Methods section for details). The post mortem MRI data are presented
132 together with the histological data for comparison (first column).

133 Based on our segmentations of the subcortical auditory structures in the post mortem MRI
134 data, the resulting 3-D model is presented in Figure 2. A volumetric quantification of the identified
135 structures (in the BigBrain and post mortem MRI) is reported in Table 1 and the overlap between
136 the segmentations computed after projection in MNI space are reported in Table 2 (as inset in
137 Figure 2).

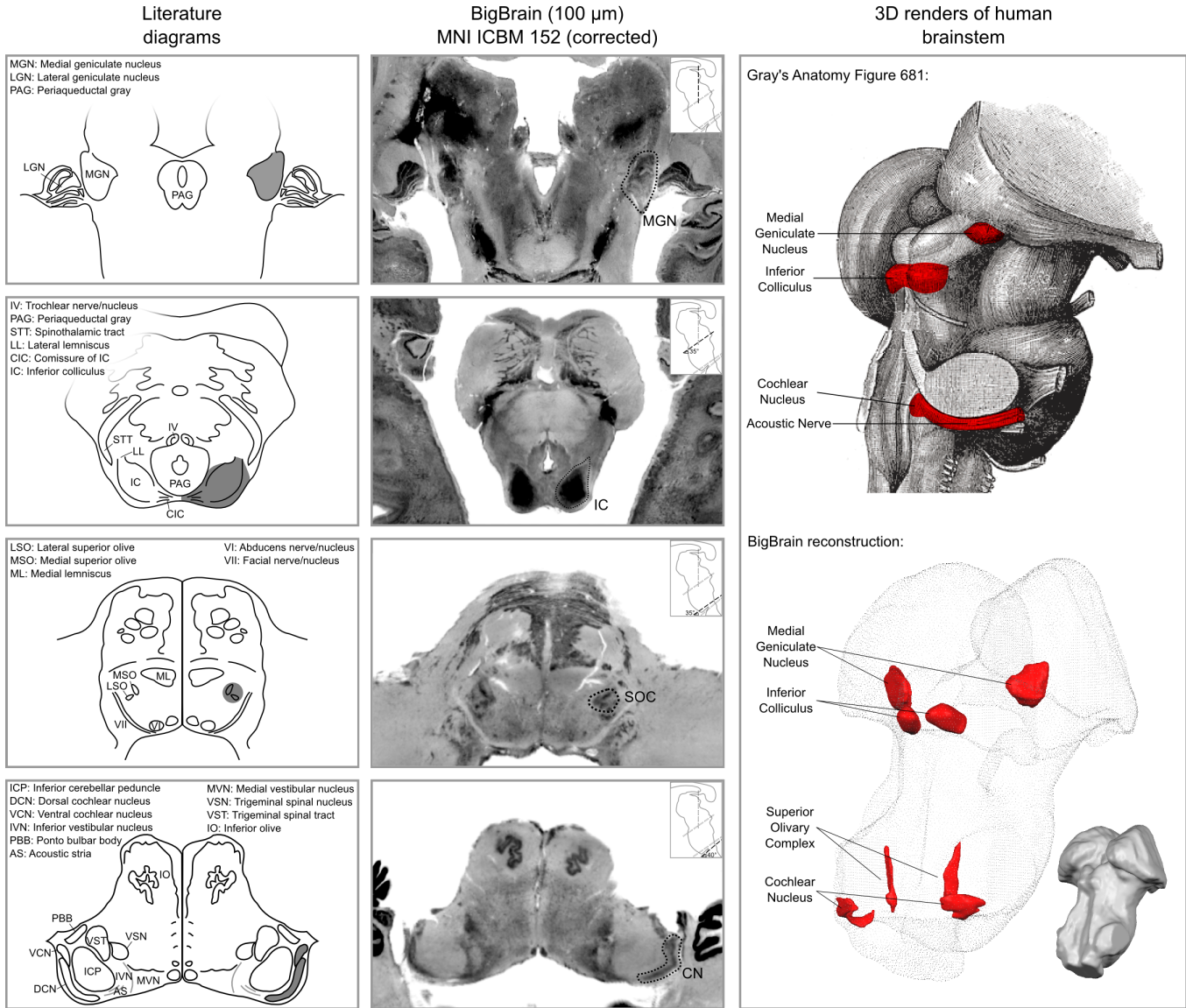


Figure 1. Literature diagrams (left columns) redrawn from *Moore (1987)* for the cochlear nucleus (CN), superior olivary complex (SOC), inferior colliculus (IC) and from the Allen Human Brain Atlas (*Hawrylycz et al., 2012*) for the medial geniculate body (MGB) compared to similar cuts from histology (BigBrain) in MNI (central column) and 3-D reconstructions of the segmented structures from the histology (bottom right column). The auditory structures are highlighted in gray in the left column, by a dotted line in the central column and in red on the modified Gray's anatomy Plate 719 (*Gray and Lewis, 1918*) and rendered as solid red surface meshes within the surface point cloud render of BigBrain MNI brainstem (right column). See *Figure 9* for 3-D animated videos of these auditory structures.

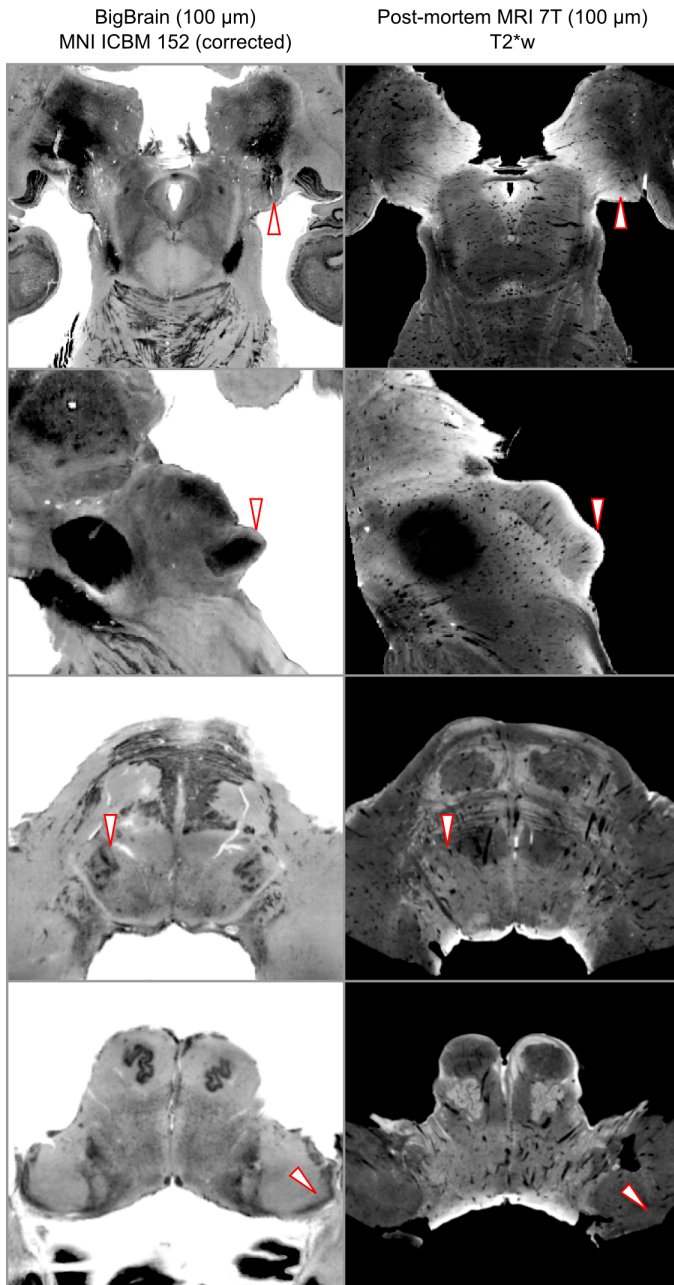


Table 2. Segmentation similarity comparison between BigBrain, post-mortem and in-vivo auditory nuclei

		DICE Coeff.		Avg. Hausdorff Dist.	
		Left	Right	Left	Right
BigBrain across segmenters	MGN	0.72	0.75	1.43	1.34
	IC	0.83	0.77	0.48	0.85
	SOC	0.61	0.51	4.30	5.80
	CN	0.80	0.74	0.77	2.63
BigBrain vs post-mortem	MGN	0.5	0.5	3.3	5.1
	IC	0.3	0.4	6.4	5.8
	SOC	0.2	0.01	5.8	7.8
	CN	0.2	0.2	7.1	6.6
BigBrain vs in-vivo	MGN	0.4	0.5	3.9	4.7
	IC	0.4	0.3	6.6	7.3
	SOC	0.1	0.03	8.9	11.5
	CN	0.04	0.1	14.6	11.6

Figure 2. BigBrain-7T post mortem MRI image comparisons. Histological data (BigBrain) (left column) and T2*-weighted post mortem MRI data (100 μm - central column) in MNI space. Panels from bottom to top are chosen to highlight subcortical auditory structures (CN [bottom] to MGB [top]). Arrows (white with red outline) indicate the location of the subcortical auditory nuclei. The 3-D structures resulting from the segmentation of the post mortem data is presented on the top right panel. Table 2 quantifies (using DICE coefficient and average Hausdorff distance) the agreement (in MNI space) for all subcortical structures between: 1) segmentations performed on the BigBrain dataset by the two raters (KS and OFG) [top]; 2) segmentations obtained from the BigBrain dataset and from the post mortem MRI data [middle]; 3) segmentations obtained from the BigBrain dataset and from in vivo functional MRI data [bottom]). See **Figure 9** for 3-D animated videos of these auditory structures.

Table 1. Comparisons between the volume (mm³) of auditory subcortical structures reported in the literature (*Glendinning and Masterton, 1998*) and the volume obtained in our BigBrain segmentation (in MNI space), post mortem MRI data segmentation and in vivo functional clusters (defined based on voxels that are significant in at least three, four, or five participants out of the ten included in Experiment 1).

	Literature	BigBrain	Post mortem	In vivo (thr=3)	In vivo (thr=4)	In vivo (thr=5)
CN	46	32	11	54	24	11
SOC	7	6	4	124	63	29
IC	65	63	73	263	189	146
MGN	58	75	134	304	207	152

138 3-D connectivity map of the human subcortical auditory system from post mortem
139 diffusion MRI

140 Identifying the connectivity between subcortical auditory nuclei is crucial for understanding the
141 structure of the pathway. However, methods for tracing neuronal pathways that are available in
142 other animal models are generally not available in human studies, even post mortem. Diffusion-
143 weighted MRI (dMRI) can be used to measure the orientation and magnitude of molecular motion
144 and infer patterns of white matter in brain tissue (both post mortem and in vivo). Using 200 μm
145 diffusion-weighted MRI data acquired on the same post mortem sample (see Methods for details),
146 we modeled diffusion orientations and estimated likely connectivity pathways (or streamlines) using
147 tractography. Constraining the streamlines to only those that pass through auditory structures (as
148 identified from the anatomical MRI data and dilated 500 μm to include adjacent white matter), we
149 visualized the connectivity map of the subcortical auditory pathway in *Figure 3*, left panel.

150 Connectivity closely resembles the expected pattern of the human subcortical auditory wiring.
151 In particular, streamlines predominantly pass through the lateral lemniscus, the primary subcortical
152 auditory tract. Additional streamlines run through the brachium of the inferior colliculus, connecting
153 the inferior colliculus with the medial geniculate of the thalamus. Many streamlines then course
154 rostrally toward the auditory cortex (not present in this specimen).

155 At the caudal extent of the lateral lemniscus, streamlines pass through the superior olivary
156 complex. Streamlines also run through the root of CNVIII. In total, each expected step along the
157 subcortical auditory pathway is represented in this connectivity map.

158 *Figure 3* (top right panel) shows the percentage of total streamlines connecting each of the
159 subcortical auditory structures as estimated from this post mortem diffusion MRI sample. Overall,
160 connections tend to be between ipsilateral structures, with weak connectivity to contralateral
161 structures other than commissural connections to the contralateral homolog (except for between
162 the cochlear nuclei). Still, the majority of streamlines pass through just one region (shown along the
163 diagonal).

164 To investigate the relationship between streamline connectivity and ROI definition strictness,
165 we conducted two additional analyses. In *Figure 3*, we dilated the anatomical ROIs by 500 μm (2.5
166 voxels at 200 μm resolution), thereby including nearby white matter tracts (as well as adjacent
167 subcortical structures). In contrast, *Figure 3–Figure Supplement 1* shows streamlines based on the
168 anatomical ROIs without dilation to account for white matter. As regions were defined as the core
169 nuclei in the anatomical MRI, they largely exclude white matter tracts (such as the lateral lemniscus
170 and brachium of the inferior colliculus), leading to much sparser connectivity between subcortical
171 auditory nuclei.

172 Next, we resampled the diffusion MRI images to an in vivo-like resolution (1.05 mm isotropic). We
173 again estimated fiber ODFs using CSD and estimated white matter connections with deterministic
174 tractography. Using the (undilated but downsampled) anatomically defined ROIs as tractogra-
175 phy waypoints, we can visualize streamline estimates connecting subcortical auditory structures
176 (*Figure 3–Figure Supplement 2*). Similar to the dilated ROI connectivity estimates, we see greater
177 ipsilateral connectivity estimates between structures, particularly between left structures.

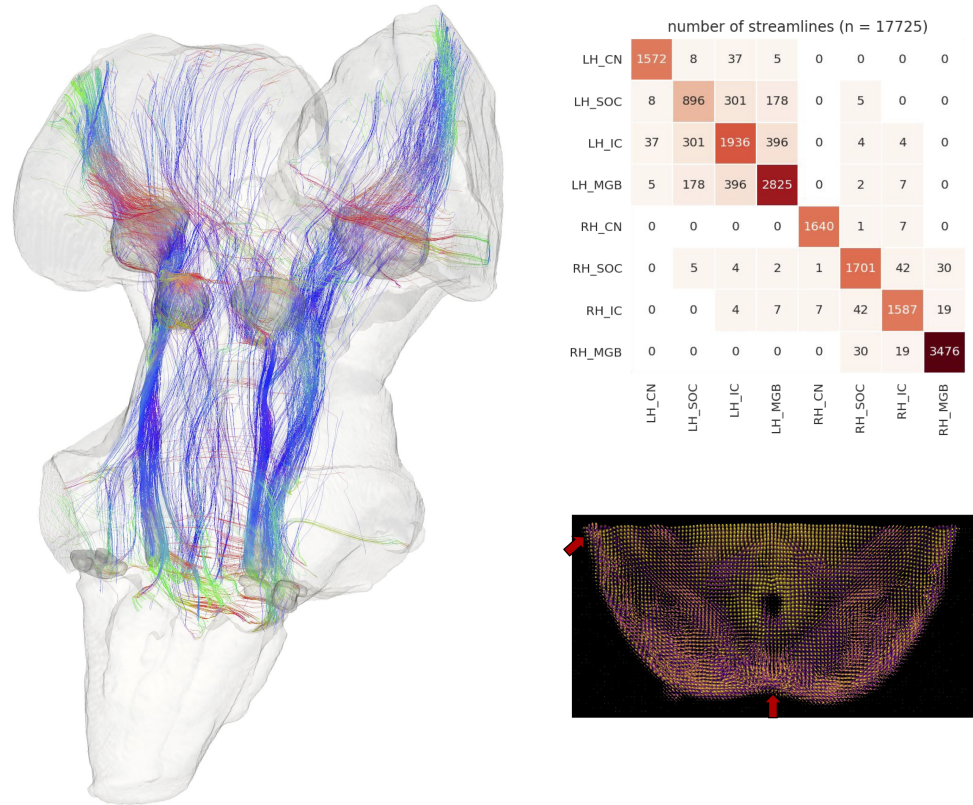


Figure 3. Post mortem diffusion MRI tractography. Left: streamlines passing through subcortical auditory structures, defined from 50 μm post mortem MRI in the same specimen, warped to 200 μm isotropic diffusion image space and dilated 2.5 voxels (500 μm) to include neighboring white matter. Colors represent the local orientation at each specific point along the streamline: blue is inferior-superior, red green is anterior-posterior, and red is left-right. Ten percent of streamlines are represented in this image. A rotating animation is available in the online resources. Top right: Connectivity heatmap of subcortical auditory structures. Bottom right: Diffusion orientation distribution functions (ODFs) for each voxel; axial slice at the level of the rostral inferior colliculus (IC), including the commissure of the IC (bottom center arrow) and brachium of the IC (top left arrow). A video of the streamlines is available online: <https://osf.io/kmbp8/>

Figure 3-Figure supplement 1. Post mortem tractography with undilated ROIs.

Figure 3-Figure supplement 2. Post mortem tractography using data downsampled to in vivo resolution (1.05 mm).

Figure 3-video 1. 360° rotation video of post mortem streamlines.

178 Vasculature representations from post mortem MRI

179 Because T2*-weighted GRE imaging is sensitive to blood vessels, we processed our anatomical
 180 MR image to highlight brainstem vasculature (*Figure 5*, right column, base image). These 3-D
 181 vasculature images bear striking resemblance to post mortem data acquired with a stereoscopic
 182 microscope after full clearing method (see *Duvernoy (2013)* for detailed diagrams of human brain-
 183 stem vasculature). These vasculature images in the MNI space can be helpful to understand the
 184 nature of the in vivo functional signals (see next section).

185 **In vivo MRI**

186 We next sought to identify the structures and connections of the human subcortical auditory
 187 system in living participants. By leveraging the increase signal and contrast to noise available at
 188 ultra-high magnetic fields (7 Tesla) (*Vaughan et al., 2001; Ugurbil et al., 2003; Ugurbil, 2016*), we
 189 collected high resolution anatomical (0.7 mm isotropic), diffusion-weighted (1.05 mm isotropic;
 190 198 diffusion gradient directions across 3 gradient strengths) and functional (1.1 mm isotropic)
 191 MRI in ten participants (see Methods for details). Leveraging the increased SNR available at high
 192 fields, we aimed to collect data that would allow a functional definition of the auditory pathway
 193 in individual participants. For this reason, we collected a large quantity of functional data in all
 194 individuals: two sessions with 12 runs each in Experiment 1 and two sessions with eight runs each
 195 in Experiment 2 (totalling 8 hours of functional data for each participant who completed both
 196 experiments). All statistical analyses were performed at the single subject level. Group analyses
 197 were used to evaluate the correspondence across subjects of individually defined regions (i.e., the
 198 definition of a probabilistic atlas across participants) as well as the ability to generalize to new
 199 participants by means of a leave-one-out analysis.

200 Anatomical MRI

201 Visual inspection and comparison to the MNI dataset (*Figure 5–Figure Supplement 2*) showed
 202 that the MGB and IC could be identified on the basis of the anatomical contrast, especially in
 203 the short inversion time T1-weighted data (*Tourdias et al., 2014; Moerel et al., 2015*). However,
 204 while the superior olivary complex (SOC) could be identified in the MNI dataset (*Figure 5–Figure*
 205 *Supplement 2*), it could not be identified in average anatomical image from our 7T data. This is
 206 possibly due to the limited number of subjects leading to the lower signal to noise in the average
 207 image. We have also explored the combination of image contrasts within each individual using a
 208 compositional method proposed in (*Gulban et al., 2018b*), but the results were inconclusive.

209 Functional MRI

210 The difficulty in delineating the CN and SOC from anatomical in vivo MRI data (see *Figure 5–Figure*
 211 *Supplement 1* for the average anatomical images obtained from our in vivo data) oriented our
 212 investigation towards the possibility to identify the subcortical auditory pathway—in vivo and in
 213 single individuals—on the basis of the functional responses to sounds. Functional responses to
 214 168 natural sounds (Experiment 1) were collected at 7T using a sparse acquisition scheme and a
 215 fast event-related design. We additionally report the reproducibility of the individual functional
 216 delineations in six out of the ten participants who participated in a follow up experiment in which
 217 responses to 96 natural sounds (Experiment 2) were collected at 7T using a sparse acquisition
 218 scheme and a fast event-related design.

219 Statistical analysis of the functional responses allowed us to define voxels with significant
 220 activation in response to sounds in each individual. Additionally, we created a probabilistic functional
 221 atlas based on the overlap of statistically significant maps across individuals (after anatomical
 222 registration to a reference subject). To evaluate the generalization to new data we also computed
 223 leave-one-out probabilistic functional atlases each time leaving one one of our participants (see
 224 Methods for details).

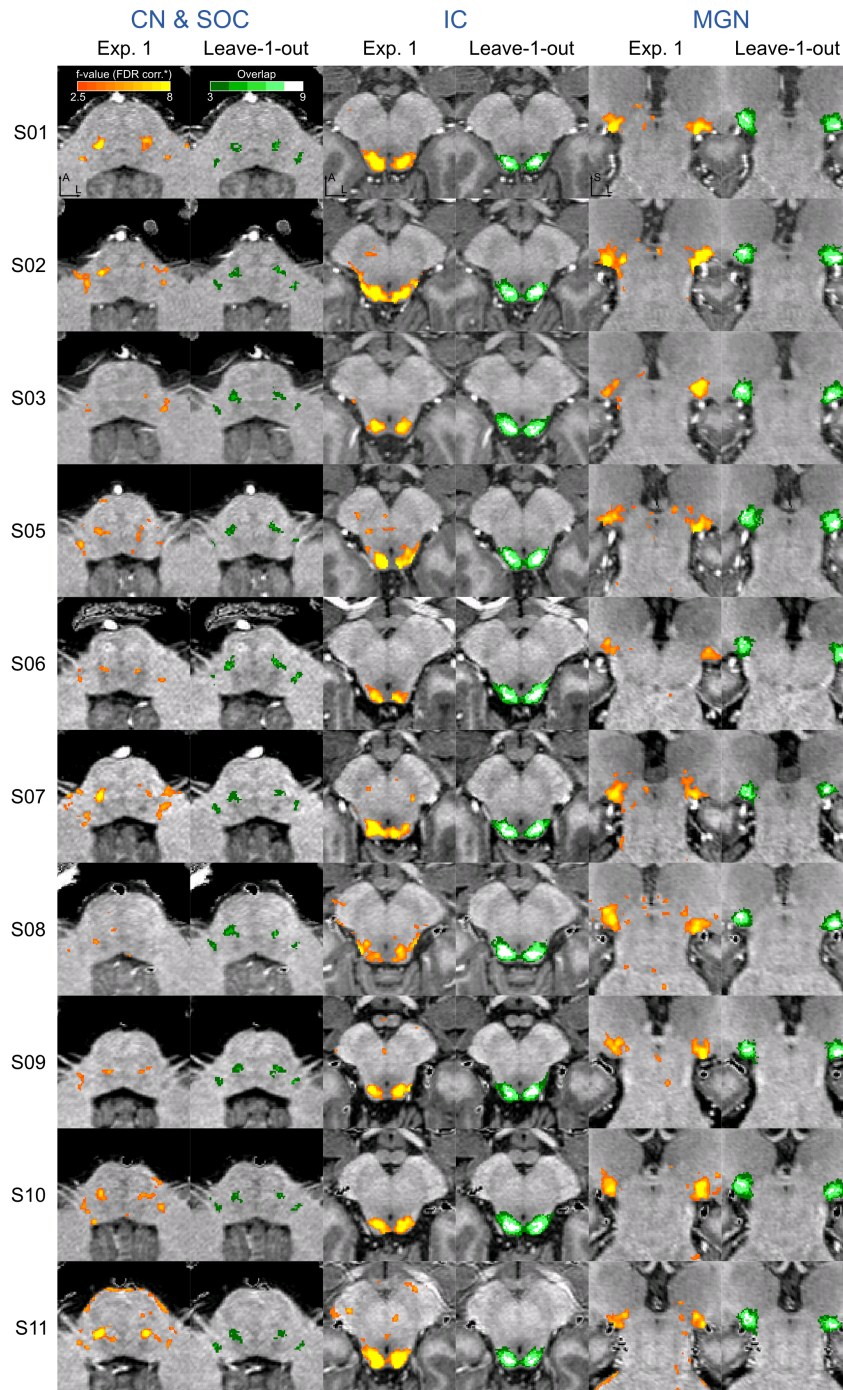


Figure 4. Single subject functional activation maps obtained from Experiment 1 thresholded for significance ($FDR-q = 0.05$ and $p < 0.001$; see Methods for details) and leave-one-out probabilistic functional maps highlighting voxels that are significant in at least three of the other nine subjects. For each participant, CN/SOC and IC are shown in transversal cuts, MGB is shown in a coronal cut. See single subject videos for 3-D view of these maps in *Figure 10* supplements. Unthresholded maps can be found in our online resources (see Data Availability section).

Figure 4–Figure supplement 1. Correspondence between single subject activation maps and leave-one-out probabilistic maps.

Figure 4–Figure supplement 2. Effect of threshold on leave-one-out probabilistic maps on correspondence with single subject activations

Figure 4–Figure supplement 3. Reproducibility across experiments of the functional activation maps in six participants (also see *Figure 11*).

Figure 4–Figure supplement 4. Correspondence between single subject activation maps across experiments.

Figure 4–Figure supplement 5. Effect of spatial smoothing in the analysis of the data collected from two of the participants.

225 **Figure 4** shows, for each individual participant, the statistically thresholded (see Methods)
 226 activation maps together with leave-one-out probabilistic functional maps obtained considering
 227 all other individuals. The unthresholded maps are reported in supplement videos to **Figure 4**
 228 and available for inspection in the online repository of the data. In all our participants, we could
 229 identify clusters of significant activation in response to sounds in the MGB, IC, SOC, and CN. In each
 230 individual and for each auditory nucleus, these activation clusters correspond to locations that are
 231 significantly active in at least three out of the other nine participants to the experiment. **Figure 4–**
 232 **Figure Supplement 1** reports the overlap and distance between functional centroids of the single
 233 subject activation maps and the leave-one-out probabilistic maps. In addition, **Figure 4–Figure**
 234 **Supplement 3** shows the reproducibility of the functional responses across experiments in six of
 235 the participants. The analysis of the overlap and distance between the centroids of activation across
 236 experiments within each of these six participants is reported in **Figure 4–Figure Supplement 4**. The
 237 higher signal-to-noise ratio attainable in regions corresponding to the IC and MGB results in highly
 238 reproducible functional responses both within and across participants in these regions. Activation
 239 clusters identified at the level of CN and SOC in single individuals also reproduce (albeit to a smaller
 240 degree with respect to IC and MGB), both within subjects (i.e., across experiments) and across
 241 subjects.

242 The left column of **Figure 5** shows the probabilistic functional map obtained from all participants
 243 in Experiment 1 (i.e., representing the number of subjects in which each voxel was identified as
 244 significantly responding to sounds-the map is thresholded to display voxels that are significantly
 245 activated in at least three out of the ten participants) overlaid on the in vivo average anatomical MRI
 246 image (short inversion time T1-weighted image (*Tourdias et al., 2014*); see Methods for details).

247 Projecting these data to the reference MNI space allowed evaluating the correspondence
 248 between in vivo functionally defined regions and histological data (Big Brain - **Figure 5**, center
 249 column).

250 At the level of the CN, the clusters of voxels active in at least three out of the ten participants
 251 correspond mostly to the ventral part of CN. The dorsal subdivision of the CN is not recovered
 252 in these probabilistic maps (at least not in at least three volunteers consistently) possibly due to
 253 partial voluming with the nearby cerebrospinal fluid in combination with thinness (thickness around
 254 0.5 mm) of the dorsal CN as it wraps around inferior cerebellar peduncle (see **Figure 1**). Nearby,
 255 the location of the activation clusters identifying the SOC overlaps with the SOC as identified in the
 256 BigBrain data.

257 As the next step, we qualitatively investigated if the orientation of the vasculature at the level of
 258 the SOC may have an effect on size (and location) of the functionally defined regions. As a visual aid
 259 in this evaluation, we overlaid the functionally defined regions with the vasculature image obtained
 260 from the post mortem data (**Figure 5**, right column). In all subcortical regions the vasculature
 261 appears to have a specific orientation, and, at the level of the SOC, vessels drain blood from the
 262 center in a ventral direction (i.e., the direction of draining is towards the surface of the brainstem in
 263 the top of the image reported in the transverse view, bottom in **Figure 5**). This specific vasculature
 264 architecture may result in the displacement or enlargement of the functionally defined clusters
 265 towards the ventral surface of the brainstem (as highlighted in the correspondence with histological
 266 data in **Figure 5**).

267 The probability of the same voxel to be significantly modulated by sound presentation across
 268 subjects increased at the level of the IC and MGB, where the histologically defined regions cor-
 269 responded (for the large part) to all subjects exhibiting significant responses to sounds. At the
 270 threshold of three subjects in the probabilistic maps, the IC seems to extend towards the superior
 271 direction, bordering and sometimes including parts of superior colliculus. On the other hand,
 272 similarly to what may happen in the SOC, the general directions of the vasculature penetrating
 273 the IC and draining blood towards the dorsal surface of brainstem angled in a superior direction
 274 (**Figure 5** right panel) may also impact the functional definition of the IC.

275 The functional responses in the MGB cover an area that is in agreement with histological data.

276 Interestingly, compared to the IC or SOC, there is no major direction of extension of functional
277 responses as well as no clear direction (in comparison to SOC and IC) of vascular draining.

278 A quantification of the volume of functionally defined structures is reported in **Table 1** for
279 different thresholds of the probabilistic group map (from a threshold that defines the regions
280 based on voxels that are significant in at least three out of the ten participants to a threshold that
281 define the regions based on voxels that are significant in at least five out of the ten participants).
282 The overlap between functional regions and the BigBrain segmentations after projection in MNI
283 space is reported in Table 2 (as bottom right inset in **Figure 2** - computed using a threshold for the
284 probabilistic maps that defines the regions based on voxels that are significant in at least three of
285 the ten participants).

286 Diffusion MRI

287 With the successful identification of the subcortical auditory structures with functional MRI, we next
288 sought to estimate the likely connections between these structures in vivo. We analyzed the high
289 spatial and angular resolution diffusion data to estimate streamlines of white matter connectivity
290 following a similar process as the post mortem MRI (see Methods for further details).

291 **Figure 6** shows diffusion tractography streamlines that pass through at least one subcortical
292 auditory structure (as defined by group-level probabilistic functional activation [significant response
293 in at least three out of ten subjects]; see section above). The high spatial and angular resolution of
294 these data allow for vastly improved estimation of white matter connections between these deep,
295 small structures.

296 While not a measure of actual physical brain connections—and therefore requiring caution in
297 interpretation—connectivity patterns resemble what we would expect to see based on animal model
298 tracer investigations. Overall, the connectivity network appears to be dominated by laterality, in that
299 left hemisphere structures are generally more connected with other left hemisphere structures.

300 However, there are a few notable exceptions to this pattern: the cochlear nuclei and superior
301 olivary complexes are strongly connected bilaterally, which fits with animal research suggesting
302 one-half to two-thirds of ascending auditory connections cross the midline at these early stages.
303 Additionally, there are a small number of connections between left and right inferior colliculi, likely
304 along the anatomical commissure of the inferior colliculus.

305 Discussion

306 The auditory pathway includes a number of subcortical structures and connections, but identifying
307 these components in humans has been challenging with existing in vivo imaging methods. We
308 showed that functional localization of the subcortical auditory system is achievable within each
309 participant, and that localization is consistent across experimental sessions. To further facilitate
310 research on the anatomy and function of the human subcortical auditory system, we created
311 3-D atlases of the human auditory pathway based on gold standard histology, 50 μm isotropic
312 resolution post mortem anatomical MRI, and in vivo functional MRI at 7T. In addition, we created
313 3-D connectivity maps of the human subcortical auditory pathway using diffusion MRI tractography
314 in a post mortem MRI sample and in living participants.

315 These atlases and connectivity maps are the first fully 3-D representations of the human
316 subcortical auditory pathway and are publicly available to make the localization of subcortical
317 auditory nuclei easier. In particular, the atlases are available in a common reference space (MNI152)
318 to make registration to other MRI data as straightforward as possible. As part of this registration
319 process, we have improved the registration of the brainstem of BigBrain histological data to the
320 MNI space, where the original MNI version presented a significant misregistration of the colliculi
321 (as noticeable in **Figure 7**). The result of our new registration allows to more correctly localize the
322 colliculi of BigBrain data in MNI without compromising the registration of other brainstem and
323 thalamic nuclei.

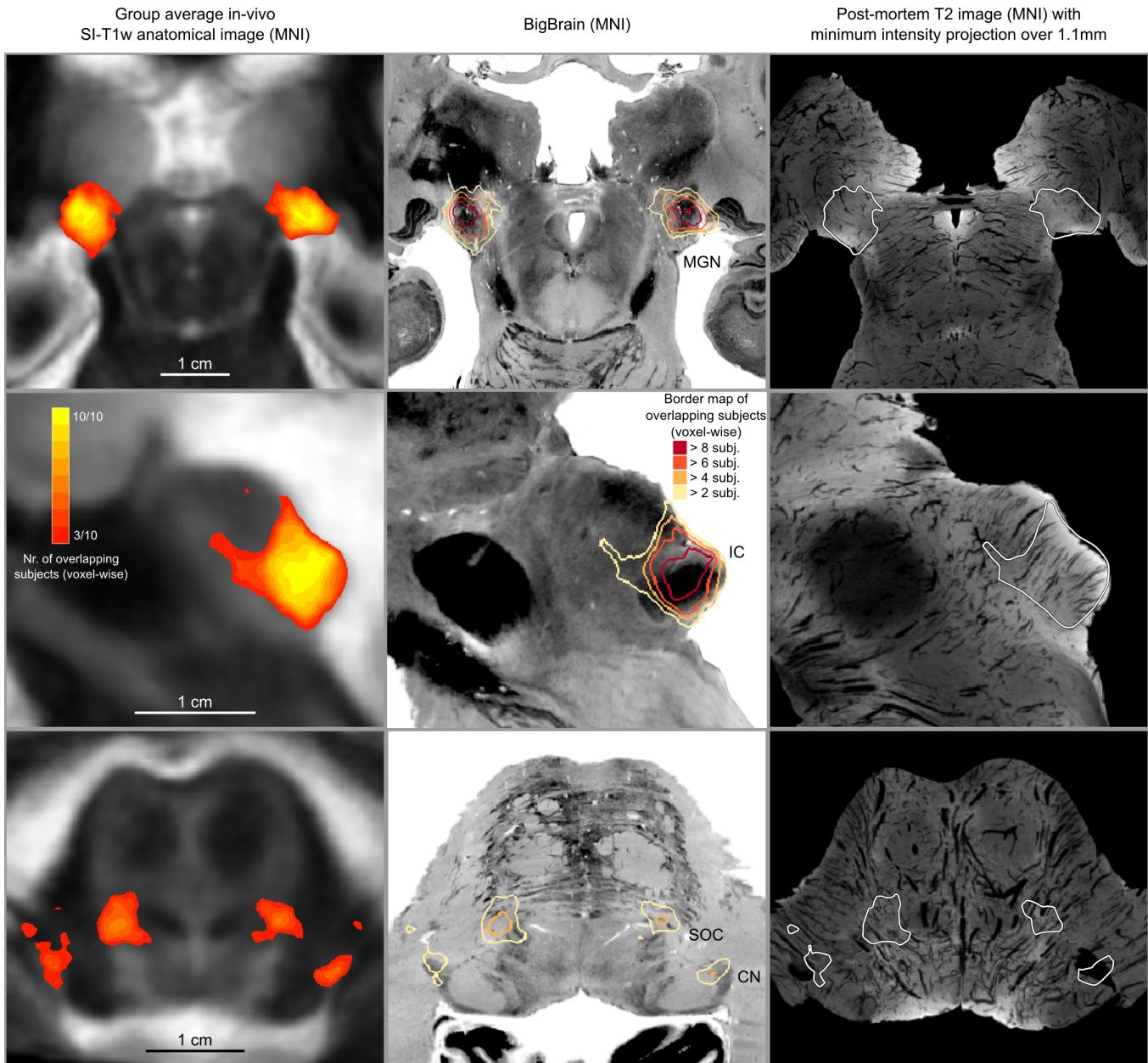


Figure 5. In vivo functional MRI responses to auditory stimuli, combined across ten participants. Left column: Conjunction of participants plotted on top of one participant's short inversion T1-weighted anatomical MRI. Center column: Conjunction of participants' fMRI responses warped to MNI space and plotted on top of BigBrain MNI (corrected) image. Right column: Conjunction of fMRI responses plotted on top of post mortem MRI vasculature images (1.1 mm minimum intensity projection).

Figure 5-Figure supplement 1. In vivo anatomical group average images in MNI space.

Figure 5-Figure supplement 2. Anatomical images from MNI ICBM 152 compared to BigBrain in MNI space

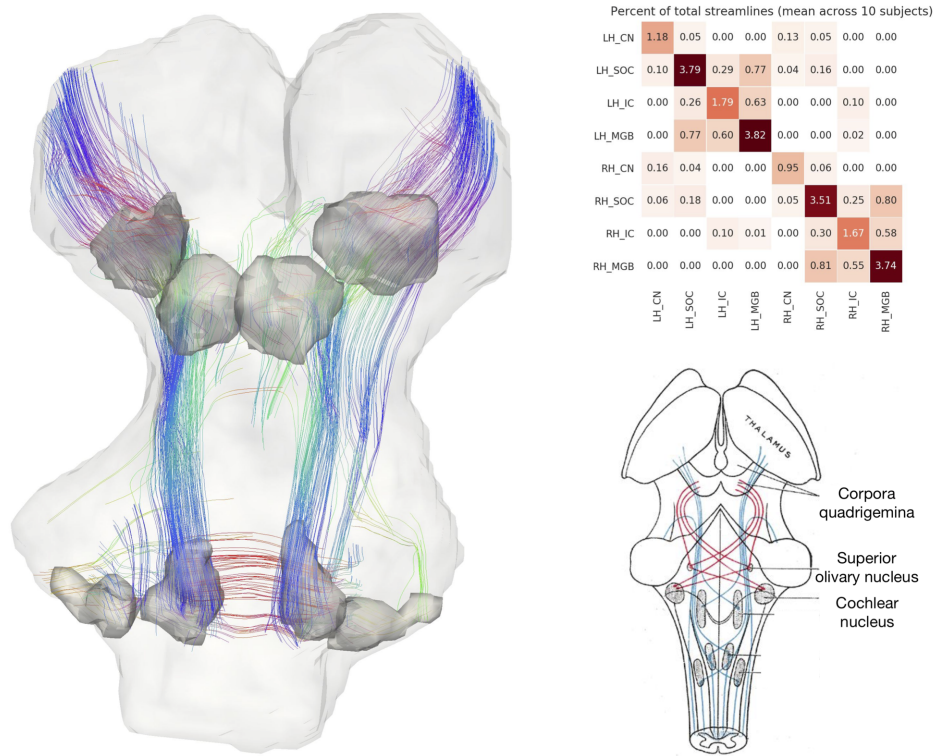


Figure 6. In vivo tractography of the subcortical auditory system from 7T diffusion-weighted MRI. Left: 3-D images from one participant. Fiber orientation distribution functions were estimated from diffusion-weighted MRI images of the brainstem and were used for deterministic tractography. Streamlines that passed through functionally defined auditory ROIs (dark grey) are shown here (excluding streamlines through the medulla). Colors represent the local orientation at each specific point along the streamline: blue is inferior-superior, red green is anterior-posterior, and red is left-right. A rotating animation is available in the online resources. Top right: connectivity between subcortical auditory ROIs as a percentage of total brainstem streamlines, averaged over 10 participants. Bottom right: schematic of auditory brainstem connectivity from Gray's Anatomy of the Human Body. A video of the streamlines is available online: <https://osf.io/ykd24/>

Figure 6–Figure supplement 1. Bar plot of streamline counts through each ROI.

Figure 6–video 1. 360° rotation video of in vivo streamlines.

324 In creating the atlas with three distinct modalities, we were able to assess the reliability of each
325 of the methods in identifying the human subcortical auditory pathway. Each modality provided
326 useful information to the segmentation of the auditory nuclei. All regions could be identified in
327 the BigBrain histological data, that also allowed us to identify small auditory sub-nuclei such as
328 the medial superior olive and lateral superior olive. High-resolution post mortem MRI also clearly
329 delineated the medial geniculate and inferior colliculus (with less contrast for the superior olive
330 and cochlear nucleus), while the overall image contrast facilitated registration with in vivo MRI.
331 High-resolution in vivo functional MRI exhibited greater sensitivity to auditory structures than in
332 vivo anatomical MRI that was even higher resolution. We showed that functional MRI is useful to
333 localize structures throughout the auditory pathway despite their small size. In each participant we
334 identified voxels significantly responding to sound presentation in regions corresponding to the CN,
335 SOC, IC and MGB. We validated these definition by evaluating both the within-subject reproducibility
336 (i.e., by comparing functional maps across two experiments in six individuals) and the ability of a
337 probabilistic atlas defined on nine out of our ten participants to generalize to the left out volunteer.

338 In total, we found that each of the methods described here provides information to the delin-
339 eation of the human subcortical auditory pathway. Our post mortem and in vivo data suggest that
340 MRI is a capable tool for investigating this system across spatial scales providing a bridge to the
341 gold standard, histology.

342 While not representing specific cells, MRI holds a number of advantages over the gold standard
343 method, histology (*Johnson et al., 1993*). First, MRI allows for visualization and analysis of an entire
344 3-D structure at once, with minimal geometric warping from (virtual) slice to slice (which can occur
345 in slice-based histology if individual slices contract on a slide or are damaged during the physical
346 slicing). Second, MRI can be used in vivo in human participants, opening up the possibility to
347 address research questions on the functional and anatomical properties of human subcortical
348 structures, their correspondence, and their involvement in human behavior.

349 Probing the connectivity of the human subcortical auditory pathway has been extremely limited,
350 since gold standard (but invasive) tracer studies are largely unavailable for human specimens. In
351 this study, we show that diffusion MRI tractography is sensitive to connections within the human
352 subcortical auditory system, both post mortem and in vivo. In addition to streamlines corresponding
353 to the lateral lemniscus—the major ascending auditory white matter tract—we can see streamlines
354 crossing the midline at the level of the superior olivary complex and the inferior colliculus.

355 Interestingly, with the highest resolution data (200 μm post mortem diffusion-weighted MRI),
356 we were able to estimate streamlines visually resembling the expected auditory pathway, but
357 missing putative key connections between subcortical auditory structures themselves when using
358 the strictly defined ROIs as tractography seeds. In contrast, the relatively lower resolution in vivo
359 diffusion-weighted MRI produced estimates of connectivity more like what we expected from the
360 literature. We had two hypotheses as to why these results appeared. First, the higher resolution
361 anatomical definition of the nuclei not including the immediately surrounding white matter could
362 miss streamlines that terminate at the immediate proximity of the structures' borders (similar
363 to issues in cortex (*Reveley et al., 2015*)). Second, partial volume effects in the lower resolution
364 data—combining white matter and grey matter in the same voxels—could actually *increase* stream-
365 lines terminating within the anatomical ROIs. Dilating the post mortem ROIs and downsampling the
366 data to the in vivo resolution both resulted in greater streamline connectivity between subcortical
367 auditory structures, suggesting that our hypotheses were likely. Thus, while high spatial resolution
368 diffusion-weighted MRI allowed for much finer, higher quality streamline estimates, it also places
369 constraints on tractography analyses that must be accounted for and investigated further.

370 More generally, the density of brainstem and midbrain nuclei and frequent crossings between
371 perpendicular white matter bundles pose a challenge to diffusion tractography estimations of white
372 matter connectivity, so it was not clear beforehand if this methodology would be sufficient for
373 visualizing these connections. Additionally, because a gold-standard connectivity method is not
374 available in humans, we could not directly validate our tractography findings (as can be done in the

375 macaque, though with limited success; see *Thomas et al. (2014)*). However, our results suggest that,
376 with continually improving diffusion-weighted MRI acquisition and analysis techniques, focused
377 investigations on the human subcortical auditory pathway can-and should-become more prominent
378 in the near future.

379 In addition to high resolution anatomical post mortem MRI and diffusion MRI tractography,
380 we were also able to identify the subcortical auditory system in vivo with functional MRI. Previous
381 studies have identified these structures with functional MRI, but they typically required constrained
382 acquisition parameters—for instance, they used single slices with low through-plane resolution
383 in order to support high in-plane resolution (*Guimaraes et al., 1998; Harms and Melcher, 2002;*
384 *Griffiths et al., 2001; Hawley et al., 2005; Sigalovsky and Melcher, 2006*). In the present study, by
385 taking advantage of the increased signal of high-field (7-Tesla) MRI, we were able to image the
386 brainstem using isotropic voxels at high resolution across a wider field-of-view that covers the
387 human auditory pathway in coronal oblique slices. The use of slice acceleration (*Moeller et al.,*
388 *2010; Setsompop et al., 2012*) allowed us to acquire enough slices to cover the whole brainstem,
389 thalamus and cortical regions around Heschl's gyrus with the exclusion of anterior portions of the
390 superior temporal gyrus and sulcus. Using isotropic voxels allowed us to better evaluate the 3-D
391 volume of significantly activated regions, limiting partial volume effects that are inevitable when
392 using thick anisotropic slices.

393 Similar to previous research at lower magnetic fields (*Hawley et al., 2005; Sigalovsky and*
394 *Melcher, 2006*), the 7T MR images did not allow for an anatomical definition of the CN and SOC
395 (although IC and MGB were clearly visible). A possible reason for this is the reduced signal- and
396 contrast-to-noise ratio in these regions. Only very recently has 7T MRI enabled anatomical localiza-
397 tion at the level of the SOC in individual subjects (*Garcia-Gomar et al., 2019*). It should be noted
398 that we could identify the SOC in the MNI ICBM 152 dataset that results from the average of a much
399 larger cohort. Therefore, future investigations should be tailored to optimize anatomical image
400 contrasts to auditory brainstem regions in single subjects. The (post mortem) atlases we provide
401 here will prove a useful tool for these investigations by providing a reference for the expected
402 location (and size) of these regions.

403 In contrast to in vivo anatomical localization, our data—in agreement with previous reports
404 (*Hawley et al., 2005; Sigalovsky and Melcher, 2006*)—show that *functional* mapping of the subcor-
405 tical auditory pathway is an effective method for localizing these structures. While histologically
406 defined CN and SOC regions have been previously used to sample functional responses from in vivo
407 fMRI data (*Hawley et al., 2005; Sigalovsky and Melcher, 2006*), the overlap between functionally
408 and histologically defined subcortical auditory structures has not been reported before. Here
409 we investigated the ability of BOLD fMRI (as an indirect measure of neuronal activity) to localize
410 subcortical auditory regions. We show that functional definitions are possible, as distinct clusters
411 of activation were detected in all subjects across the subcortical auditory pathway. These regions
412 were reproducible both within subjects (across experiments) and across subjects (comparing single
413 participants functional maps to the leave-one-out atlas obtained with all other participants). We
414 could identify the subcortical auditory nuclei despite not using cardiac gating, a method that previ-
415 ous studies showed to increase the signal-to-noise ratio in subcortical regions (*Guimaraes et al.,*
416 *1998; Harms and Melcher, 2002; Griffiths et al., 2001; Hawley et al., 2005; Sigalovsky and Melcher,*
417 *2006*). We instead increased statistical power by presenting a large number of natural sounds
418 with multiple repetitions. Using smaller voxels also reduced partial volume effects between cere-
419 brospinal fluid (which is heavily affected by physiological noise) and the brain tissue (*Triantafyllou*
420 *et al., 2016*). In addition, the correspondence of functionally defined regions across ten participants
421 after anatomical alignment allowed us to build a functional probabilistic atlas.

422 Despite these positive outcomes, functionally defined regions exhibited overall larger volumes
423 compared to the histological ones (see Table 1 in *Table 1*). Although we acquired data at relatively
424 high resolution (1.1 mm isotropic), our functional voxel size and the mild spatial smoothing (1.5mm)
425 might be the source of this observation. Another factor that may have impacted the increased

426 volume of the in vivo probabilistic regions can be the residual anatomical misalignment across
427 subjects that also contributes especially to the lower degree of overlap at CN and SOC. In this case,
428 the individual anatomical images not showing enough contrast might be the cause. Partial volume
429 also most likely impacted small regions such as the CN and SOC, and draining effects due to the
430 vascular architecture could also have an impact on the size and localization of the in vivo defined
431 regions. Further, because we used only the overall response to sounds as functional definition, the
432 regions we defined may include sub-regions not specific to the system under investigation (e.g., the
433 inclusion of multisensory deep layers of the superior colliculus at the border with the IC) (*Sparks
434 and Hartwich-Young, 1989; Jiang et al., 1997*). This effect could be reduced by using different
435 stimuli and statistical contrasts. For instance, one could contrast uni-sensory and multi-sensory
436 stimuli to identify—within the current functional definition—the IC voxels that respond to visual
437 stimulation and thus may represent multi-sensory superior colliculus. For the IC and MGB, where
438 signal-to-noise ratio in the functional data is larger, a higher threshold in the probabilistic maps
439 results in a more accurate volumetric definition as well as more correct anatomical localization (see,
440 e.g., *Figure 5*). It should also be noted that direct comparison of post-mortem and in vivo results
441 suffers from the additional problem of aligning data with very diverse contrasts and resolutions.
442 For the IC and MGB our procedure could be verified on the basis of the anatomical contrast in the
443 in vivo data, for the CN and SOC the lack of anatomical contrast (to be leveraged by the alignment
444 procedure) in the in vivo data may be the source of some of the misalignment between the data.

445 We also investigated the possibility of defining anatomical connections between subcortical
446 auditory nuclei using diffusion-weighted MRI. While affected by similar confounds as functional
447 MRI (e.g., partial voluming effects, physiological noise, and relative signal weighting), this technique
448 faces additional complications introduced by the number of orientations required, the gradient
449 strength (b-value) selected, the modeling of diffusion or fiber orientations within each voxel, and
450 the estimation of streamlines across brain regions, especially within the subcortical auditory sys-
451 tem (*Zanin et al., 2019*). The post mortem and in vivo diffusion MRI datasets in this study each
452 implemented state-of-the-art acquisition techniques to optimize the MRI signal-to-noise ratio and
453 minimize MRI modeling errors. For example, as the fixation process likely changes the diffusion
454 characteristics of the tissue (*Pfefferbaum et al., 2004; Miller et al., 2011*), we compensated for this
455 effect by increasing the diffusion gradient strength (b-value). The constrained spherical deconvolu-
456 tion modeling method takes advantage of the high angular resolution of each dataset to provide
457 fine-grained estimations of fiber orientation distributions. Additionally, the Euler Delta Crossings
458 (EuDX) deterministic tractography method is effective at generating streamlines through voxels with
459 multiple fiber orientation peaks, such as where white matter bundles cross. However, as diffusion
460 MRI and tractography are not measuring true neuronal connections, there is still room for error in
461 diffusion orientation and streamline estimation (*Schilling et al., 2019a,b*).

462 Our BigBrain histological segmentations are very similar in volume to those reported previously
463 in the literature (*Moore, 1987; Glendinning and Masterton, 1998*), with slightly smaller cochlear
464 nuclei and slightly larger medial geniculate bodies, but similar SOC and IC volumes. It has to be
465 noted that the physical slicing process potentially introduces deformations in the tissue, and while
466 the publicly available BigBrain dataset is of extremely high quality (with good registration from
467 slice to slice), subtle deformations may have affected the shape or volume of the structures we
468 identified.

469 Post mortem MRI segmentations differed more greatly, with smaller CN and SOC definitions but
470 larger MGB definitions compared to both the literature and BigBrain histological segmentations.
471 These differences could possibly be caused by the reduced contrast-to-noise ratio in the post
472 mortem MRI data compared to the histological data (despite their high spatial resolution). This
473 reduced contrast-to-noise ratio may be caused by both reduced differences in magnetic properties
474 between the regions and their surrounding tissues as well as from residual partial volume effects
475 (especially for the very small sections of the dorsal CN, for example) that may have blurred the
476 borders of the auditory nuclei in the post mortem MRI data. Contrast-to-noise ratio may be

477 ameliorated by different acquisition/reconstruction techniques (*Wang et al., 2018*), and optimizing
 478 parameters may improve the definition of auditory nuclei on the basis of post mortem MRI data.
 479 Finally, slight misregistration between specimens (e.g. the histological data and the post mortem
 480 MRI data) likely still affect our comparisons, as registration between images (particularly from
 481 different modalities) remains a challenge. For instance, *Figure 2* shows slightly different shapes
 482 and locations for the inferior colliculus between the two datasets, despite non-linear registration to
 483 the same template. Although non-linear methods significantly improve gross registration between
 484 specimens, large misregistrations are still possible (as shown for the colliculi in the original BigBrain
 485 MNI registration). These issues can be addressed manually using additional image registration
 486 techniques, as we did here with the BigBrain MNI registration (see our "corrected" version above),
 487 but such hands-on, time-intensive edits are not always possible. Further, vastly different image
 488 contrasts (like histology and MRI) result in different regions or subregions being emphasized in the
 489 signal, creating an additional challenges in the registration procedure.

490 More generally, post mortem imaging—whether MRI or histology—is prone to modest defor-
 491 mation of the specimen. Additionally, both post mortem specimens in this paper (BigBrain and
 492 post mortem MRI) were from 65-year-old male donors, and age may have additionally affected the
 493 volume of the brain structures we investigated.

494 Despite these limitations, the inter-rater and inter-experiment reliability in this study suggest
 495 that each method is effective for localizing the subcortical auditory pathway. The reliable functional
 496 localization of subcortical auditory structures opens the door to future investigations of more
 497 complex human auditory processing. The atlases derived from each localization method is publicly
 498 available (see "Data and code availability" in Methods) to facilitate further investigations into the
 499 structure, function, and connectivity of the human subcortical auditory system in vivo. Lastly, the
 500 3-D representations found in this paper and in the available data should be beneficial to others
 501 in understanding the immensely complex, but identifiable, structure of the human subcortical
 502 auditory pathway.

503 **Methods**

504 See Supplementary *Figure 8* for a summary of data sources, data processing steps, and software
 505 used in these analyses.

506 **MRI acquisition parameters**

507 **In vivo MRI**

508 The experimental procedures were approved by the ethics committee of the Faculty for Psychology
 509 and Neuroscience at Maastricht University (reference number: ERCPN-167_09_05_2016), and were
 510 performed in accordance with the approved guidelines and the Declaration of Helsinki. Written
 511 informed consent was obtained for every participant before conducting the experiments. All
 512 participants reported to have normal hearing, had no history of hearing disorder/impairments or
 513 neurological disease.

514 Images were acquired on a 7T Siemens MAGNETOM scanner (Siemens Medical Solutions,
 515 Erlangen, Germany), with 70 mT/m gradients and a head RF coil (Nova Medical, Wilmington, MA,
 516 USA; single transmit, 32 receive channels) at Maastricht University, Maastricht, Netherlands.

517 We conducted two separate experiments. In Experiment 1, data were collected for $n=10$ partici-
 518 pants (age range 25 to 30, 6 females), in three separate sessions. In the first session, we acquired
 519 the in vivo anatomical data set consisting of: 1) a T1-weighted (T1w) image acquired using a 3-D
 520 MPRAGE sequence (repetition time [TR] = 3100 ms; time to inversion [TI] = 1500 ms [adiabatic
 521 non-selective inversion pulse]; echo time [TE] = 2.42 ms; flip angle = 5°; generalized auto-calibrating
 522 partially parallel acquisitions [GRAPPA] = 3 (*Griswold et al., 2002*); field of view [FOV] = 224 × 224
 523 mm²; matrix size = 320 × 320; 256 slices; 0.7 mm isotropic voxels; pixel bandwidth = 182 Hz/pixel;
 524 first phase encode direction anterior to posterior; second phase encode direction superior to

525 inferior); 2) a Proton Density weighted (PDw) image (0.7 mm iso.) with the same 3-D MPRAGE
 526 as for the T1w image but without the inversion pulse (TR = 1380 ms; TE = 2.42 ms; flip angle =
 527 5°; GRAPPA = 3; FOV = 224 × 224 mm²; matrix size = 320 × 320; 256 slices; 0.7 mm iso. voxels;
 528 pixel bandwidth = 182 Hz/pixel; first phase encode direction anterior to posterior; second phase
 529 encode direction superior to inferior); 3) a T2*-weighted (T2w) anatomical image acquired using
 530 a modified 3-D MPRAGE sequence (*De Martino et al., 2015*) that allows freely setting the TE (TR =
 531 4910 ms; TE = 16 ms; flip angle = 5°; GRAPPA = 3; FOV = 224 × 224 mm²; matrix size = 320 × 320;
 532 256 slices; 0.7 mm iso. voxels; pixel bandwidth = 473 Hz/pixel; first phase encode direction anterior
 533 to posterior; second phase encode superior to inferior) and 4) a T1-weighted images acquired with
 534 a short inversion time (SI-T1w) using a 3-D MPRAGE (*Tourdias et al., 2014*) (TR = 4500 ms; TI = 670
 535 ms [adiabatic non-selective inversion pulse]; TE = 3.37 ms; flip angle = 4°; GRAPPA = 3; FOV = 224
 536 × 224 mm²; matrix size = 320 × 320; 256 slices; 0.7 mm isotropic voxels; pixel bandwidth = 178
 537 Hz/pixel; first phase encode direction anterior to posterior; second phase encode direction superior
 538 to inferior). To improve transmit efficiency in temporal areas when acquiring these anatomical
 539 images we used dielectric pads (*Teeuwisse et al., 2012*).

540 In the same session we acquired, for each participant, a diffusion-weighted MRI data set using a
 541 multi-band diffusion-weighted spin-echo EPI protocol originating from the 7T Human Connectome
 542 Project (1.05 mm isotropic acquisition and b-values = 1000 and 2000 s/mm²) (*Vu et al., 2015*),
 543 extended in order to collect one additional shell at b-value at b = 3000 s/mm² (*Gulban et al.,*
 544 *2018a*). Other relevant imaging parameters were (FOV = 200 × 200 mm² with partial Fourier 6/8,
 545 132 slices, nominal voxel size = 1.05 mm isotropic, TR/TE = 7080/75.6 ms, MB = 2, phase encoding
 546 acceleration (GRAPPA) = 3, 66 directions and 11 additional b = 0 volumes for every b-value). A
 547 total of 462 volumes were obtained (231 in each phase encoding direction anterior-posterior and
 548 posterior-anterior) for a total acquisition time of 60 minutes.

549 The other two sessions were used to collect functional data in order to identify sound responsive
 550 regions in the human thalamus and brainstem. Participants listened to 168 natural sounds (1
 551 second long) coming from seven categories (speech, voice, nature, tools, music, animals and
 552 monkey calls) presented in silent gaps in between the acquisition of functional volumes and were
 553 asked to press a button every time the same sound was repeated. The experimental paradigm
 554 followed a rapid-event-related design in which sounds were presented with a mean inter stimulus
 555 interval of four volumes (minimum three maximum five volumes). The two sessions were identical
 556 and each session consisted of twelve functional runs and across the twelve runs each sound was
 557 presented three times (i.e., each sounds was presented six times across the two sessions). The 168
 558 sounds were divided in four sets of 42 sounds, each set was presented in three (non consecutive)
 559 runs. As a result, the twelve functional runs of each session formed four cross validation sets each
 560 one consisting of nine training runs and three testing runs (i.e., 126 training and 42 testing sounds).
 561 Note that the testing runs were non overlapping across the cross validations. Catch trials (i.e., sound
 562 repetitions) were added to each run, and were excluded from all analyses.

563 Functional MRI data were acquired with a 2-D Multi-Band Echo Planar Imaging (2D-MBEPI)
 564 sequence (*Moeller et al., 2010; Setsompop et al., 2012*) with slices prescribed in a coronal oblique
 565 orientation in order to cover the entire brainstem and thalamus and covering primary and secondary
 566 cortical regions (TR = 2600 ms; Gap = 1400 ms ; TE = 20 ms; flip angle = 80°; GRAPPA = 3; Multi-Band
 567 factor = 2; FOV = 206 × 206 mm²; matrix size = 188 × 188; 46 slices; 1.1 mm isotropic voxels; phase
 568 encode direction inferior to superior). Reverses phase encode polarity acquisitions were used for
 569 distortion correction. Respiration and cardiac information were collected during acquisition using a
 570 respiration belt and pulse oximeter respectively.

571 In experiment 2, six of the volunteers that participated in experiment 1 were recalled and
 572 functional data were acquired with the same slice prescription and functional MRI parameters as in
 573 experiment 1 (2D-MBEPI; TR = 2600 ms; Gap = 1400 ms ; TE = 20 ms; flip angle = 80°; GRAPPA = 3;
 574 Multi-Band factor = 2; FOV = 206 × 206 mm²; matrix size = 188 × 188; 46 slices; 1.1 mm isotropic
 575 voxels; phase encode direction inferior to superior). Experiment 2 consisted of two sessions

576 in which participants listened to 96 natural sounds (1 second long) coming from six categories
 577 (speech, voice, nature, tools, music, animals) together with ripples (bandwidth = 1 octave; center
 578 frequency = [300 Hz, 4 kHz]; AM rate = [3 Hz, 10 Hz]). Some ripple sounds contain a short noise
 579 burst ('target') and participants were asked to detect such target in either low frequency ripples
 580 or high frequency ripples in the two sessions respectively (the target occurrence varied (70 vs. 30
 581 percent) for ripples whose center frequency did or did not match the current attention condition).
 582 All sounds were presented in silent gaps in between the acquisition of functional volumes. The
 583 experimental paradigm followed a rapid-event-related design in which sounds were presented
 584 with a mean inter stimulus interval of four volumes (minimum three maximum five volumes). The
 585 two sessions consisted of eight functional runs and across the eight runs each natural sound was
 586 presented three times (i.e., each sounds was presented six times across the two sessions) while the
 587 ripples were presented seven times per run. The 96 natural sounds were divided in four sets of
 588 24 sounds, each set was presented in two (non consecutive) runs. As a result, the eight functional
 589 runs of each session formed four cross validation sets each one consisting of six training runs
 590 and two testing runs (i.e., 72 training natural sounds and 24 testing natural sounds). Note that
 591 the testing runs were non overlapping across the cross validations. In each session of experiment
 592 two we also collected a lower resolution (1 mm isotropic) anatomical reference images (T1 and PD
 593 weighted) using the 3D MPRAGE sequence for alignment purposes and included reverses phase
 594 encode polarity acquisitions for distortion correction. Respiration and cardiac information were
 595 collected during acquisition using a respiration belt and pulse oximeter respectively.

596 Both in-vivo datasets acquired for experiment 1 and experiment 2 have never been published
 597 before. This is the first work that uses this dataset.

598 Post mortem MRI

599 A human brainstem and thalamus specimen were dissected at autopsy from a 65-year-old anony-
 600 mous male. The specimen was flushed with saline and immersed for two weeks in 10% solution of
 601 neutral buffered formalin. Following this, the specimen was re-hydrated for one week in 0.1 M solu-
 602 tion of phosphate buffered saline doped with 1% (5 mM) gadoteridol. Before the MRI acquisition,
 603 the specimen was placed in custom MRI-compatible tube immersed in liquid fluorocarbon.

604 Magnetic resonance imaging was conducted in a 210 mm small-bore Magnex/Agilent MRI at the
 605 Duke University Center for In Vivo Microscopy. 3-D gradient echo images were collected at $50 \mu\text{m}^3$
 606 spatial resolution over a period of fourteen hours, with FOV = $80 \times 55 \times 45$ mm, repetition time (TR)
 607 = 50 ms, echo time (TE) = 10 ms, flip angle = 60° , and bandwidth = 78 Hz/pixel.

608 Diffusion-weighted spin echo images were collected at $200 \mu\text{m}^3$ spatial resolution with 120
 609 diffusion gradient directions at strength $b=4000 \text{ s/m}^2$ and 11 $b=0 \text{ s/m}^2$ volumes over 208 hours.
 610 The FOV was $90 \times 55 \times 45$ mm with TR = 100 ms, TE = 33.6 ms, and bandwidth = 278 Hz/pixel.

611 Anatomical image registration

612 SI-T1w, T1w, T2*w and PDw images ($700 \mu\text{m}$ iso.) were transformed to Talairach space ($500 \mu\text{m}$
 613 iso.) using BrainvoyagerQX version 2.8.4 (Goebel, 2012). Intensity inhomogeneity correction as
 614 implemented in SPM12 unified segmentation (Ashburner and Friston, 2005) was used for all images.
 615 A smaller volume containing brainstem and thalamus in each image was extracted (in the Talairach
 616 space) using FSL version 5.0.9 (Jenkinson et al., 2012) and histogram matched using percentile
 617 clipping (1% and 99%).

618 Individual masks for each 10 brainstems were created semi-automatically using ITK-SNAP
 619 version 3.6.0 active contour segmentation mode followed by manual edits. These masks included
 620 regions starting from 2 cm below the inferior part of pons to 0.5 cm above the medial geniculate
 621 nucleus (MGN), with a lateral extend reaching until the lateral geniculate nucleus (LGN) and 3 cm
 622 anterior from MGN, not including cerebellum or large arteries that lie on the surface of brainstem.
 623 These brainstem masks were then used with FSL-FNIRT (Andersson et al., 2007) to warp nine of
 624 the ten brainstems to the reference brainstem (subject 1) using SI-T1w images. We used the SI-

625 T1w images to drive the non linear registration due to the enhanced anatomical contrast across
 626 structures within the thalamus and brainstem present in these images (*Tourdias et al., 2014*;
 627 *Moerel et al., 2015*). The FNIRT parameters were subsamp = 2, 2, 1, 1, miter = 100, 100, 50, 50,
 628 infwhm = 2, 2, 1, 1, reffwhm = 2, 2, 0, 0, lambda = 100, 50, 20, 5, estint = 0, 0, 0, 0, warpres = 2, 2, 2 with
 629 spline interpolation (parameters not mentioned here were the defaults as set in FSL 5.0.9).

630 To compare in vivo with post mortem MRI and histology data, we projected the averaged SI-T1w,
 631 T1w, T2*w and PDw images to the MNI reference space (ICBM 152 2009b non-linear symmetric,
 632 500 µm iso.) (*Fonov et al., 2009, 2011*)¹. The ICBM 152 reference includes T1w, T2w and PDw data
 633 and projecting in vivo and post mortem MRI as well as histology data to this space allowed us also
 634 to evaluate the contrast that these commonly used template images have in subcortical auditory
 635 areas. To register our in vivo MRI data set to MNI, we used FSL-FNIRT but this time driven by the
 636 T1w images (available both in our data set and in the MNI ICBM 152 2009b data).

637 The post mortem diffusion b0 image was transformed to the post mortem anatomical image
 638 space with an affine transformation in ANTs. Anatomical-space images (including the manually
 639 segmented atlas) could then be transformed into diffusion space using the 'antsApplyTransforms'
 640 command, with the affine transform matrix, a super-sampled diffusion image (from 200 µm to 50
 641 µm to match the anatomical image resolution) as the reference image, and denoting the warp as
 642 an inverse transform.

643 In vivo and post mortem images were registered non-linearly using ANTs. The in vivo SI-T1w
 644 image was warped to the post mortem diffusion b0 image following a rigid, then affine, then
 645 non-linear SyN algorithm. This produced an in vivo brainstem image in post mortem diffusion
 646 space.

647 The ANTs non-linear registration also created warp and inverse warp transforms that could then
 648 be used to transform atlases from one space to another. To preserve the higher resolution of the
 649 post mortem MRI when inverse warping post mortem images to in vivo space, we supersampled
 650 the in vivo SI-T1w image to 200 µm (matching the post mortem diffusion image) or 50 µm (matching
 651 the post mortem anatomical image).

652 Finally, to transform the post mortem anatomical image (50 µm) to MNI space, we applied the
 653 inverse transform from post mortem anatomical to diffusion space (resampled to 50 µm), then the
 654 inverse transform from diffusion space to in vivo space (similarly upsampled to 50 µm), and finally
 655 from in vivo space to MNI space using the FSL-FNIRT inverse transform (described above).

656 **BigBrain histology segmentation**

657 In what follows we describe the main anatomical observations related to the auditory structures
 658 as segmented in the 100 µm histological data. Images were segmented independently by two
 659 raters (KRS, OFG). Overlap between the two raters was high (see Table 2 [top row - Big Brain across
 660 segmenters] in *Figure 2*); in the figures we show the regions that were consistently segmented by
 661 both raters.

662 **Vestibulocochlear nerve**

663 The vestibulocochlear nerve (the eighth cranial nerve, or CNVIII) enters the brainstem where
 664 the medulla and the pons meet (the pontomedullary junction). The cochlear component of the
 665 vestibulocochlear nerve is composed of spiral ganglion neurons, whose cell bodies are within the
 666 cochlea and which carry frequency-specific information to the brainstem.

667 In the BigBrain histology, CNVIII extends primarily laterally (but also anteriorly and inferiorly)
 668 from the pontomedullary junction, bound posteriorly by the cerebellum. Parts of the nerve root are
 669 still visible in the images although being cut. It is therefore not labeled in our histological atlas (but
 670 see the post mortem MRI atlas below).

¹<http://www.bic.mni.mcgill.ca/ServicesAtlases/ICBM152Nlin2009>

671 Cochlear nucleus

672 Once reaching the brainstem, the auditory nerves split into two main routes—one to the anterior
673 ventral cochlear nucleus (AVCN), and one to the posterior ventral cochlear nucleus (PVCN) and then
674 on to the dorsal cochlear nucleus (DCN) (*Webster, 1992*). Within each subnucleus, the neurons
675 maintain the tonotopic frequency representation they receive from the cochlea via the cochlear
676 nerve (*De No, 1933b,a; Rose et al., 1960; Sando, 1965; Evans, 1975; Ryugo and May, 1993; Ryugo
677 and Parks, 2003*) (see bottom panels of the two left most columns in *Figure 2*).

678 In the BigBrain data, the AVCN is situated anterior and medial to the root of CNVIII, while the
679 PVCN continues from the root of CNVIII and extends posteriorly towards the DCN. The DCN is clearly
680 visible as a dark band wrapping around the cerebellar peduncle posteriorly, becoming exposed on
681 the dorsal surface of the pons.

682 Superior olivary complex

683 The next structure along the auditory pathway is the superior olivary complex (SOC), which in
684 humans is located in the inferior pons. The SOC receives the majority of its ascending inputs
685 from the contralateral cochlear nucleus, although it also receives ipsilateral inputs as well. The
686 contralateral dominance is maintained throughout the remaining ascending pathway. The SOC is
687 comprised of the lateral superior olive (LSO), medial superior olive (MSO), and the medial nucleus
688 of the trapezoid body (MNTB). The size of each of these nuclei varies between species, and it
689 is debated whether the trapezoid body exists in the human SOC (*Moore, 1987; Strominger and
690 Hurwitz, 1976*) (but see *Kulesza and Grothe (2015)* review of recent findings affirming the existence
691 of the human MNTB).

692 Although the individual substructures within the SOC have unique anatomy that can be identified
693 from histology (*Moore, 1987; Kulesza, 2007*), here we outline the structure of the SOC as a whole
694 in order to include all identifiable substructures (namely the MSO and LSO - see second panel
695 from the bottom of the two left most columns in *Figure 1*). The MSO is the largest SOC nucleus in
696 humans, unlike in other animals. The MSO receives inputs from both the left and right AVCN and
697 sends outputs to the ipsilateral lateral lemniscus. The LSO receives inputs from the ipsilateral AVCN
698 and from the ipsilateral MNTB. Outputs are sent to both ipsilateral and contralateral lateral lemnisci.
699 The MNTB receives inputs from the contralateral AVCN, and its axons terminate in the ipsilateral
700 LSO.

701 The MSO and LSO are visible in the BigBrain images, despite their small size. The MSO is a
702 thin pencil-like collection of nuclei whose caudalmost point begins around the same axial plane
703 as the rostralmost extent of the AVCN, about 4 mm medial (and slightly anterior) to the AVCN. It
704 then extends about 1 cm rostrally (angled slightly laterally), where it eventually meets the lateral
705 lemniscal tract. The LSO neighbors the MSO near its caudalmost portion, forming a "V" shape
706 when viewed axially. In our histological atlas, these two structures are combined into a single SOC
707 segmentation. Cells of the MNTB are not clear to us in this sample, so we do not segment it in our
708 atlas.

709 Inferior colliculus

710 The inferior colliculus (IC) is a large, spherical structure in the dorsal midbrain and receives ascending
711 inputs from the auditory brainstem via the lateral lemniscus (see second panel from the top of the
712 two left most columns in *Figure 1*). The central nucleus of the inferior colliculus receives most of
713 these connections, with external nuclei primarily receiving descending connections (*Webster, 1992*).
714 The inferior colliculus sends axons to the medial geniculate body of the thalamus via the brachium
715 of the inferior colliculus.

716 In the BigBrain data, the inferior colliculus is clearly identifiable as the lower two of the four
717 bumps along the dorsal portion of the midbrain (or tectum). The darkest staining within these
718 structures corresponds to the central nucleus of the inferior colliculus. An intensity gradient
719 outside of the central nucleus likely corresponds to the external and dorsal nuclei, which were

720 included in our segmentation of the IC. Bounding the IC superiorly is the superior colliculus;
 721 medially, the commissure of the IC connecting the two inferior colliculi, as well as the aqueduct and
 722 periaqueductal grey; and anteriorly, other midbrain nuclei such as the cuneiform nucleus (lateral
 723 and inferior to the IC are the borders of the midbrain).

724 Medial geniculate of the thalamus

725 The medial geniculate body (MGB) of the thalamus is the final subcortical auditory structure that
 726 sends auditory signals to the auditory cortex via the acoustic radiations (*Winer, 1984*) (see top panel
 727 of the two left most columns in *Figure 1*). The MGB contains two or three major subdivisions: the
 728 ventral MGB receives the majority of IC inputs, while the dorsal and medial subdivisions (at times
 729 grouped together, at times separately) receive more varied inputs from auditory and non-auditory
 730 subcortical structures.

731 In the BigBrain sample, the MGB is visible as a dark patch medial to the lateral geniculate nucleus
 732 (which can be easily identified by its striations) in a coronal view. Axially, the MGB takes an ovoid
 733 shape with a clear dorsolateral boundary next to the brachium of the superior colliculus, which
 734 appears light due to lack of cell nuclei being stained. Ventromedially, the MGB is bordered by a light
 735 band corresponding to the medial lemniscus. Rostrally, we marked the edge of the MGB where cell
 736 staining decreases, at the border with the pulvinar nucleus and ventral posterolateral nucleus of
 737 the thalamus.

738 Post mortem MRI segmentation

739 In what follows we describe the anatomical contrast that can be leveraged from these post mortem
 740 MRI data in order to identify structures in the auditory brainstem. We then used these segmenta-
 741 tions to create an MRI-based atlas of the subcortical auditory system, separate from the BigBrain
 742 histology-based atlas.

743 Vestibulocochlear nerve

744 The CNVIII is visible in the post mortem MRI near the pontomedullary junction, extending laterally
 745 and anteriorly from the brainstem (see the lower panels in *Figure 2*).

746 Cochlear nucleus

747 The cochlear nuclei are challenging to identify in the post mortem MRI data, although the presence
 748 of the CNVIII root provides a landmark for localizing the other structures. Due to low signal contrast
 749 around the ventral cochlear nucleus area in the T2*-weighted GRE MRI, we segmented the VCN
 750 according to the literature: bound by the cochlear nerve root and wall of the pons laterally, and
 751 by cerebellar white matter tracks medially. We were able to segment the dorsal cochlear nucleus
 752 based on the T2*-weighted image, where it appears brighter and can be identified as running
 753 posteriorly from the VCN and dorsally along the surface of the pons, distal to the inferior cerebellar
 754 peduncle.

755 Superior olivary complex

756 As with the cochlear nuclei, the SOC are more difficult to identify in the post mortem MRI than in the
 757 histology, likely since the individual subnuclei like the MSO and LSO approach the size of a voxel in
 758 at least one direction and are therefore prone to partial voluming effects. However, the pencil-like
 759 MSO can still be identified in the coronal plane as a dark, elongated structure in the T2*-weighted
 760 image, starting around the level of the ventral cochlear nucleus. In the axial plane, the SOC (but not
 761 its individual subnuclei) can be seen as a dark spot in the T2*-weighted image between the facial
 762 nucleus and the trapezoid body (see the second row from the bottom in *Figure 2*).

763 Inferior colliculus

764 As in the BigBrain data, the inferior colliculus is relatively easy to identify based on its gross
 765 anatomical structure on the dorsal aspect of the midbrain. Additionally, the MR contrast provides

766 relatively clear boundaries between the colliculi and surrounding structures. Indeed, it may even
 767 be possible to segment the inferior colliculus into its subnuclei—the central, external, and dorsal
 768 nuclei—based on T2*-weighted MR signal intensities (see the second row from the top in *Figure 2*).
 769 The external nucleus of the IC appears dark in the T2*-weighted image, on the lateral aspect
 770 of the IC. Medial to the external nucleus is the central nucleus, which has higher T2*-weighted
 771 intensity (appears brighter) in our MR images, and has clear boundaries on its ventral, medial, and
 772 dorsolateral sides. The dorsal nucleus is along the dorsal aspect of the IC and is the brightest
 773 subcomponent within the IC in terms of T2*-weighted MR signal.

774 Medial geniculate

775 Although the borders of the MGB are less clear in the post mortem MRI than in the BigBrain images,
 776 the structure itself is again relatively easy to identify by its gross anatomical location as well as
 777 MR signal intensity. In the coronal plane, the medial geniculate is medial to the lateral geniculate
 778 at the junction of the midbrain and thalamus. Axially, the medial geniculate has circular or ovoid
 779 shape, again medial to the lateral geniculate. In the axial plane, the medial geniculate is largely
 780 bordered dorsolaterally by the brachium of the superior colliculus, which appears as a thick, dark
 781 band of fibers in the T2*-weighted image. Medially, the medial geniculate is bound by the brachium
 782 of the inferior colliculus (also appearing as a dark fiber band), at least through the caudal half
 783 of the structure. We have included the portions of this fiber bundle in the segmentation of the
 784 medial geniculate, as the auditory fibers connecting the IC and the MGB are quite relevant to MRI
 785 connectivity investigations (including our own; post mortem tractography results below).

786 As with the inferior colliculus, it may be possible to identify separate divisions within the medial
 787 geniculate. Within the overall structure, there are two identifiable substructures based on T2*-
 788 weighted MR image intensity. Dorsomedially (and somewhat caudally), about half of the medial
 789 geniculate has high T2*-weighted contrast and appears bright; the ventrolateral (and slightly rostral)
 790 half appears darker in the T2*-weighted image. These segmentations largely (but not perfectly)
 791 align with the ventral and dorsal/medial nuclei of the medial geniculate in the Allen Human Brain
 792 Atlas (*Hawrylycz et al., 2012*), as well as with those of *Paxinos et al. (2019)*. However, they vary
 793 somewhat from the the axial slice segmentation from *Merker (1983)* shown in *Amunts et al. (2012)*,
 794 which show a largely horizontal delineation between the substructures.

795 Functional MRI analysis

796 In both functional experiments, data were preprocessed using BrainvoyagerQX version 2.8.4
 797 (*Goebel, 2012*). Slice-scan-time correction, motion correction, temporal high-pass filtering (GLM-
 798 Fourier, 6 sines/cosines) and temporal smoothing (Gaussian, width of kernel 5.2 s). The defaults
 799 in BrainvoyagerQX v2.8.4 were used for these steps aside from the explicitly stated values. The
 800 functional images were then distortion corrected using the opposite phase encoding direction
 801 images using FSL-TOPUP (*Andersson et al., 2003*). Conversion between Brainvoyager file types
 802 to NIfTI which was required to perform distortion correction was done using NeuroElf version
 803 1.1 (release candidate 2)² in Matlab version 2016a. For alignment across experiments (i.e., to
 804 co-register the data of experiment 2 to the ones collected in experiment 1) we used FSL-FLIRT. In
 805 this procedure the alignment between the functional data of the two experiments was tailored to a
 806 mask that included the brainstem, thalamus and auditory cortex.

807 After pre-processing, functional images were then transformed to Talairach space using Brain-
 808 voyager at a resolution of 0.5 mm isotropic. We have previously used this procedure in order to
 809 reveal tonotopic maps in both the inferior colliculus and medial geniculate nucleus (*De Martino*
 810 *et al., 2013; Moerel et al., 2015*) and have shown that the upsampling has no consequence on the
 811 spatial distribution of the responses. Upsampling can also reduce effects of interpolation that
 812 is common during resampling in many image processing steps. After upsampling, mild spatial
 813 smoothing (Gaussian, FWHM 1.5mm) was also applied. *Figure 4–Figure Supplement 5* shows the

²<http://neuroelf.net/>

814 effect that spatial smoothing has on the activation maps obtained from two participants data in
815 experiment 1.

816 GLM-denoise (*Kay et al., 2013*) was used to estimate noise regressors. In brief, for each cross
817 validation a noise pool of non responsive voxels (i.e., voxels with a response to sound representation
818 determined by an F-statistic below a given threshold) was determined on the training data set (16
819 runs across the two sessions of experiment 1 and 12 runs across the two sessions of experiment 2)
820 and used to obtain noise regressors defined as the principal components of the noise pool time
821 course matrix that added to a GLM analysis (*Friston et al., 1994*) of the training data would result
822 in an increased activation. The number of noise regressors was optimized using cross validation
823 within the training set. The selected noise regressor spatial maps were projected on the test data to
824 obtain the regressors for the test data.

825 Similarly, the hemodynamic response function (HRF) best characterizing the response of each
826 voxel in the brainstem was obtained using a deconvolution GLM (with 9 stick predictors) on the
827 training data. Note that this procedure, while possibly overfitting information in the training data,
828 produces noise regressors and an HRF for each test run (e.g. the noise regressors for runs 4, 6 and
829 9 of session one in experiment 1 comes from an analysis performed on all other runs in the same
830 session) that are not overfitted.

831 The resulting HRF and noise regressors were used in a GLM analysis of the test runs. We
832 combined all test runs (for each individual voxel) using a fixed effect analysis.

833 Statistical maps of responses to sounds vs silence were corrected for multiple comparisons
834 at the individual level using False Discovery Rate (FDR; $q\text{-FDR} = 0.05$). An additional threshold on
835 the uncorrected p-value of each voxel (i.e., $p < 0.001$) was applied to further reduce the number of
836 false positive activation that can be expected when applying FDR. Unless otherwise stated, single
837 subject statistical maps are displayed by color coding voxels that surpass these statistical thresholds.
838 Unthresholded statistical maps are visualized in **Figure 10** and are available at the online repository
839 of the data (https://osf.io/hxeKn/?view_only=be9ec398304344e8bb694a0658d77ed6) for inspection.

840 The functional activation maps of the six participants that took part in both experiments have
841 been analyzed to demonstrate within participant reproducibility of effects. Since the stimuli were dif-
842 ferent and the number of runs were different, this second experiment shows a generalization of the
843 first experiment, thereby additionally validating the detection of these structures. **Figure 4–Figure**
844 **Supplement 3** shows the statistically thresholded activation maps for each of this six participants
845 for the two experiments in three anatomical cuts (two transversal for CN/SOC and IC and one
846 coronal for the MGB). The percentage of statistically significant voxels in experiment 1 that are
847 statistically significant in experiment 2 is reported together with the distance between the centroids
848 of activations between the two experiments in **Figure 4–Figure Supplement 4** (for each individual
849 and in average across individuals). The unthresholded maps of both experiments (for each of
850 the six participants) are also visualized in **Figure 11** and are available at the online repository
851 (https://osf.io/hxeKn/?view_only=be9ec398304344e8bb694a0658d77ed6) for inspection.

852 To produce group level results, the single subject statistical maps were warped to the reference
853 brainstem (subject 1) by applying the warping field obtained on the anatomical data. After projection
854 to the common space, single subject statistical maps were binarized and converted to a probabilistic
855 map by: 1) applying of a cluster size threshold of 3.37 mm^3 (27 voxels in the 0.5 mm isotropic
856 anatomical space 2.5 voxels in the original functional resolution) and 2) summing maps across
857 subjects at each single voxel (i.e., a value of 10 indicates that all 10 subjects exhibited a statistically
858 significant response to sound presentation corrected for multiple comparisons and belonging to
859 a cluster of at least 27 voxels in the anatomical space). The additional clustering allowed us to
860 further control for possible false positives by imposing a neuroanatomically plausible hypothesis
861 (i.e., none of our region of interest is smaller than 3.37 mm^3 in volume). The same procedure was
862 also repeated by leaving one subject out (i.e., we generated probabilistic maps from 9 out of the
863 ten subjects each time leave one subject out). The leave-one-out probabilistic maps were then
864 back-projected to the anatomical space of the left out subject (i.e., the probabilistic map obtained

865 from subjects 1 to 9 was back-projected to the anatomical space of subject 10). Unless otherwise
 866 stated, probabilistic maps are displayed with minimum threshold of at least three out of ten (or nine
 867 for the leave one out maps) subjects exhibiting significant responses at each voxel. Unthresholded
 868 probabilistic maps are available for inspection at the online repository.

869 We evaluated how well cluster localized on the basis of our probabilistic maps generalize
 870 to new data. **Figure 4** displays the statistically thresholded activation maps for each of the ten
 871 participants in experiment 1 in three anatomical cuts (two transversal for CN/SOC and IC and one
 872 coronal for the MGB) together with the probabilistic map obtained from the other nine participants
 873 (thresholded by displaying voxels that are functionally significant in at least three out of nine
 874 participants). In **Figure 4–Figure Supplement 1** we report the percentage of voxels in the leave
 875 one out probabilistic maps that are statistically significant in the left out subject. The overlap
 876 is reported together with the distance between the centroids of activations in the leave one
 877 out probabilistic maps and the left out subject. The effect of the threshold on the probabilistic
 878 maps is analyzed in **Figure 4–Figure Supplement 2**. The unthresholded maps (leave one subject
 879 out and single subject) are also visualized in **Figure 10** and available at the online repository
 880 (https://osf.io/hxekn/?view_only=be9ec398304344e8bb694a0658d77ed6) for inspection.

881 To compare the functional activation maps with histology data and post mortem MRI data, the
 882 probabilistic maps were projected to the MNI space using the warping field obtained from the
 883 anatomical dataset.

884 **BigBrain data**

885 Histology data were obtained by downloading the 100 μm version of the BigBrain (*Amunts et al.,*
 886 **2013**) 3-D Volume Data Release 2015 (from <https://bigbrain.loris.ca>). We downloaded both the
 887 original images and the dataset already aligned to MNI ICBM 152. The nuclei along the auditory
 888 pathway (cochlear nucleus, superior olive, inferior colliculus and medial geniculate nucleus) were
 889 manually segmented in the histology space image using ITK-SNAP (*Yushkevich et al., 2006*) largely
 890 following the definitions in *Moore (1987)* when possible.

891 **Correction of the alignment of the inferior colliculi to MNI**

892 Upon visual inspection of the BigBrain image in the MNI ICM 152 space, we detected a major regis-
 893 tration error around the inferior colliculi (see **Figure 7** - second panel from the left). The registration
 894 quality to MNI ICMBM 152 space in the rest of the brainstem was deemed satisfactory, but the the
 895 region of the inferior colliculus required correction in order to perform a valid comparison with the
 896 MRI data (in vivo and post mortem). Interestingly, the region of the colliculi of the BigBrain in the
 897 original histology space appeared to be closer in location to the position of the inferior colliculus in
 898 the MNI dataset (compare panel 1 and 3 in **Figure 7**) indicating that the highlighted misalignment
 899 in the original BigBrain MNI dataset originated during the registration procedure.

900 To perform a new registration to MNI of the brainstem and thalamus of the BigBrain data that
 901 observed the already correctly registered boundaries (e.g. the Pons) but corrected the region
 902 around the inferior colliculus bilaterally, we followed N steps. First, we defined a region of interest
 903 around the inferior colliculus using common anatomical landmarks that were visible in the BigBrain
 904 MNI and MNI (2009b) T1, PD, T2 images and where aligned satisfactorily. Second, this region was cut
 905 out from the BigBrain MNI and replaced by the same region (i.e., defined by the same anatomical
 906 landmarks) in the BigBrain histology space data (before projection to MNI). The convex hulls of the
 907 region of interest in the BigBrain histology and in the MNI space were matched using 3-D optimal
 908 transport as implemented in Geogram version 1.6.7 (*Lévy, 2015; Lévy and Schwindt, 2018*). Third,
 909 the convex hull matched region of the the BigBrain histology space was used to replace the incorrect
 910 region which was cut out at step 2. As a result of these three steps we obtained a version of the
 911 BigBrain in MNI (BigBrain MNI - implanted) that had the inferior colliculus in the right position but
 912 where the transitions between outside to inside of the region of interest that was corrected were
 913 visible and not respecting of the topology. To correct for these residual errors, we performed a

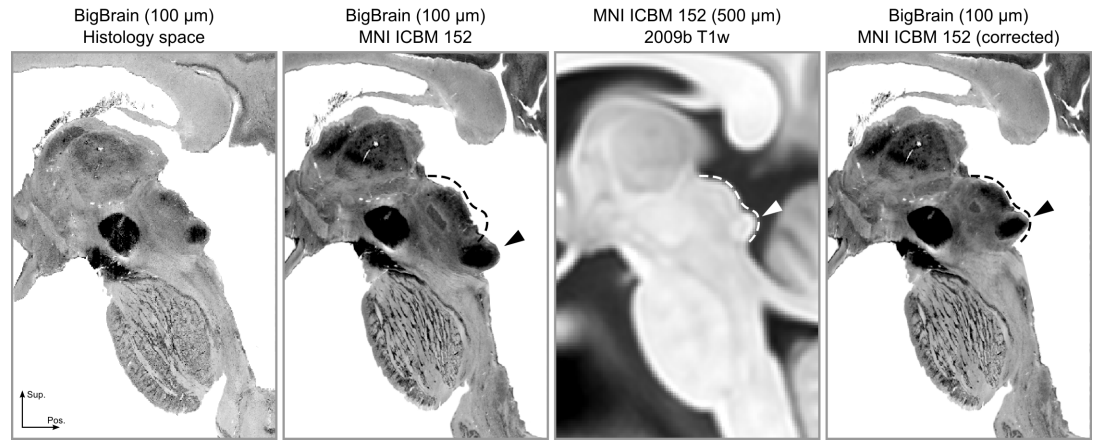


Figure 7. The registration error around the inferior colliculus is visible bilaterally when comparing Panel 2 and Panel 3. The dashed lines indicate the correct shape (and location) of the colliculi in MNI space. The arrows point to the inferior colliculus (IC). The last panel shows the corrected BigBrain MNI dataset.

914 new FSL-FNIRT alignment between the original BigBrain in histology space and the BigBrain MNI
 915 - implanted image. The resulting image (BigBrain MNI - corrected) preserved the actual topology
 916 inside the brainstem and at the same time resulted in a correct alignment of the regions around
 917 the inferior colliculus bilaterally (see *Figure 7* - right panel).

918 **Post mortem MRI vasculature analysis**

919 Gradient echo (GRE) MRI is sensitive to vasculature within the imaged tissue. To highlight vasculature
 920 in the post mortem brainstem specimen, we computed the minimum intensity projection in coronal
 921 sagittal and axial direction from the 50 μm isotropic voxel GRE MRI data over slabs of 1.1 mm in
 922 thickness using Nibabel (*Brett et al., 2017*) and Numpy (*Van Der Walt et al., 2011*). This image can
 923 be seen in *Figure 5* right column.

924 **Diffusion MRI analysis**

925 Post mortem diffusion

926 Before analysis, post mortem diffusion volumes were each registered to the first b_0 volume using
 927 an affine transformation in ANTs version 2.1.0 (*Avants et al., 2011*). To estimate white matter fiber
 928 orientations, we used the constrained spherical deconvolution (CSD) model as implemented in DIPY
 929 0.14 (*Gorgolewski et al., 2011; Garyfallidis et al., 2014; Tournier et al., 2007*) as a Nipype pipeline
 930 (*Gorgolewski et al., 2011*). CSD posits that the observed diffusion signal is a convolution of the
 931 true fiber orientation distribution (FOD) with a response function. DIPY's 'auto-response' function
 932 estimates the fiber response function from a sphere of 10 voxels in the center of the sample above
 933 a given fractional anisotropy (FA) threshold (0.5 in our study). We then estimated FOD peaks in
 934 each voxel using DIPY's 'peaks-from-model' method with a 10° minimum separation angle and a
 935 maximum of 5 peaks per voxel.

936 White matter fiber streamlines were estimated deterministically with DIPY's EudX method (*Mori*
 937 *et al., 1999; Garyfallidis, 2013*) with 1,000,000 seeds per voxel, a 75° streamline angle threshold,
 938 and an FA termination threshold of 0.001 (since data outside the specimen sample were already
 939 masked to 0).

940 To define regions of interest (ROIs) for the fiber display, the auditory structures manually
 941 delineated in the post mortem T2*-weighted MR images were transformed to diffusion space
 942 using ANTs, and global streamlines were filtered by considering only the voxels in each one of the
 943 ROIs as a seed and further constrained by using all auditory ROIs as tractography waypoints. This
 944 resulted in a high-resolution, high-quality auditory-specific subcortical tractogram, which were then
 945 visualized in TrackVis 0.6.1 (*Wang et al., 2007*).

946 In vivo diffusion

947 7T in vivo dMRI data was corrected for distortions with the HCP pipeline *Glasser et al. (2016);*
 948 *Sotiropoulos et al. (2013)*. Specifically, geometric and eddy-current distortions, as well as head
 949 motion, were corrected by modeling and combining data acquired with opposite phase encoding
 950 directions *Andersson et al. (2003); Andersson and Sotiropoulos (2015, 2016)*. The data were then
 951 masked to include just the brainstem and thalamus, matching the post mortem specimen.

952 Similar to the post mortem analysis, we estimated diffusion FODs with a CSD model imple-
 953 mented in DIPY with response function FA threshold of 0.5. Peaks were extracted with a minimum
 954 separation angle of 25°. White matter connectivity was estimated with deterministic tractography
 955 throughout the brainstem and thalamus, again using DIPY's EudX algorithm (*Mori et al., 1999;*
 956 *Garyfallidis, 2013*) with 1,000,000 seeds per voxel, a 45° streamline angle threshold, and an FA
 957 termination threshold of 0.023.

958 For the tractography in the in vivo data we used subcortical auditory ROIs as defined by the
 959 analysis of the functional data (i.e., regions that exhibited significant [corrected for multiple com-
 960 parisons] response to sound presentation in at least three out of ten subjects). The functional
 961 ROIs were transformed to individual diffusion space and used as tractography seeds, with all other
 962 auditory ROIs as waypoints, producing a subcortical auditory tractogram for each in vivo subject.

963 **Data and code availability**

964 Unprocessed in vivo data are available at (<https://openneuro.org/datasets/ds001942>). Atlas seg-
 965 mentations and tractography streamlines are available through the Open Science Framework
 966 (<https://osf.io/hxekn/>). Processing and analysis resources, including links to all data and software
 967 used in this paper, are available at <https://github.com/sitek/subcortical-auditory-atlas> (*Sitek and*
 968 *Gulban, 2019*). See *Figure 8* for an overview of currently available data and code (full resolution
 969 version available at our code repository).

970 **Animated 3D volume renderings**

971 Video animations in *Figure 9*, *Figure 10* and *Figure 11* were created using pyqtgraph (v0.10.0,
 972 <http://www.pyqtgraph.org/>) volume rendering. The t-value maps were clipped to 0-20 range and
 973 scaled to 0-255 range. These t-values are 3D volume rendered by assigning the corresponding gray
 974 value to each voxel as well as the alpha channel (transparency). Which means that lower values are
 975 closer to black and translucent. Animation frames were generated by rotating camera one degree
 976 at a time for 360 degrees. Additive rendering was used for 2D projections to provide depth vision
 977 (i.e., for preventing voxels closest to the camera from seeing values inside the clusters.).

978 **Acknowledgements**

979 We would like to thank to Christophe Lenglet for helping with in vivo dMRI processing and analysis
 980 and Marta Bianciardi, Jean Augustinack, and George Paxinos for giving anatomical advice at various
 981 stages. F.D.M. and O.F.G. were supported by NWO VIDI grant 864-13-012. S.S.G. and K.R.S. were
 982 supported by NIH grant 5R01EB020740. S.S.G. was also supported by P41EB019936. K.R.S. was
 983 additionally funded by NIH NRSA fellowship 5F31DC015695, the Amelia Peabody Scholarship from
 984 the Eaton Peabody Laboratory at Mass. Eye and Ear (Boston, MA, USA), and a travel grant from
 985 the Harvard Brain Science Institute. MR Histology was acquired at the Duke Center for In Vivo
 986 Microscopy, an NIH/NIBIB National Resource (P41EB015897 to G.A.J.), NIH 1S10OD010683-01 (to
 987 G.A.J.).

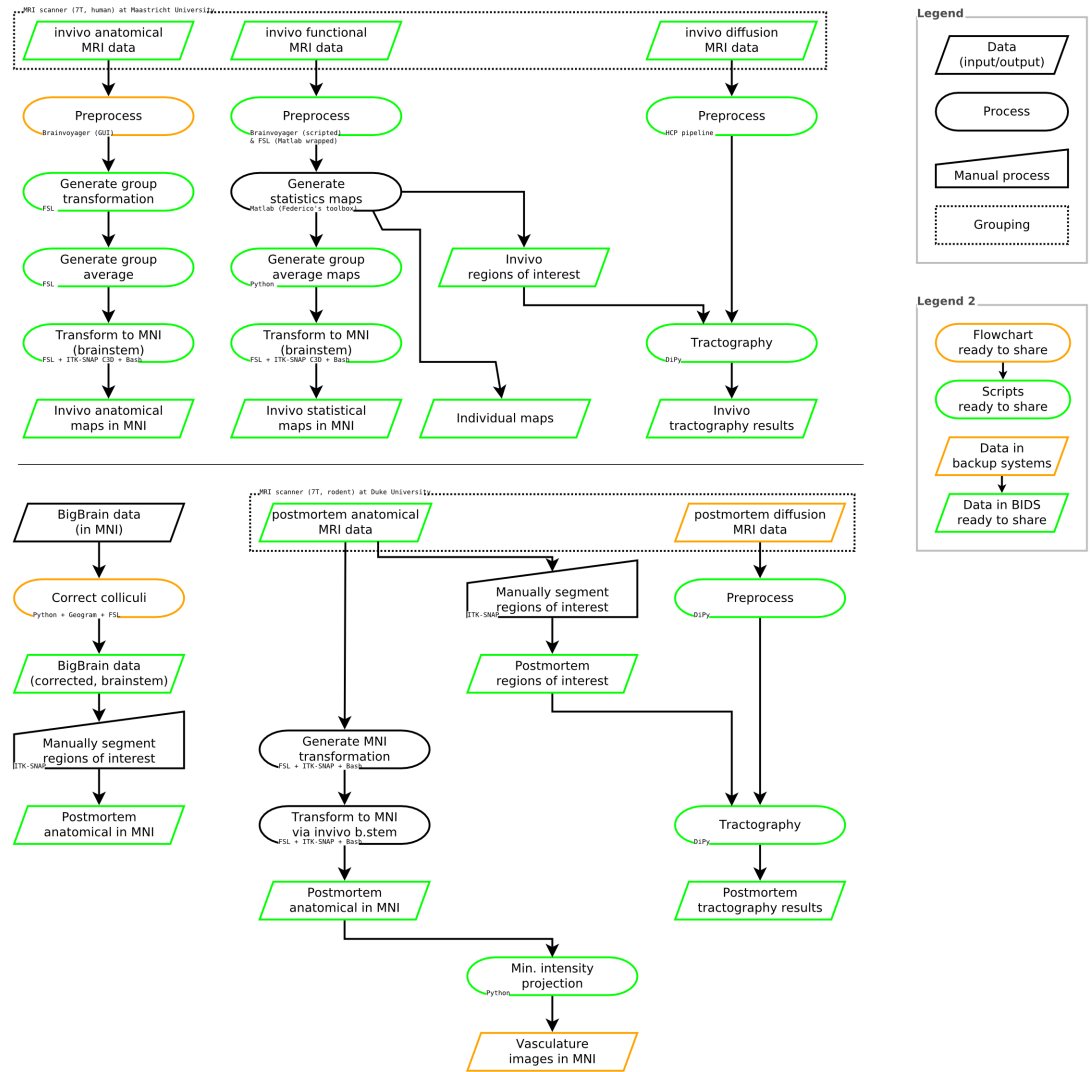


Figure 8. Summary of data processing steps, including availability of data and code.

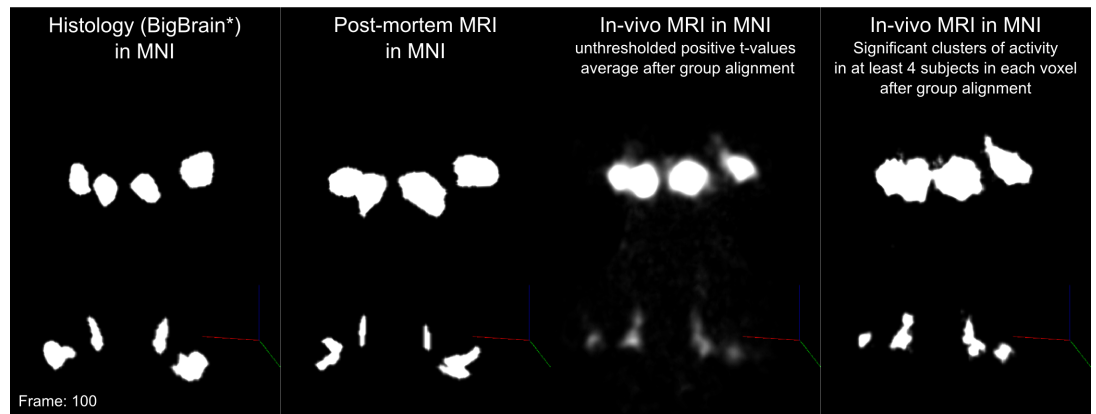


Figure 9. One frame of volume rendered animations for comparing histology (BigBrain), post-mortem MRI, in-vivo MRI unthresholded positive t-values group average and in-vivo MRI clusters of significant activity overlapping in at least 4 subjects in each voxel.

Figure 9–video 1. 3D volume rendered comparisons in MNI space.

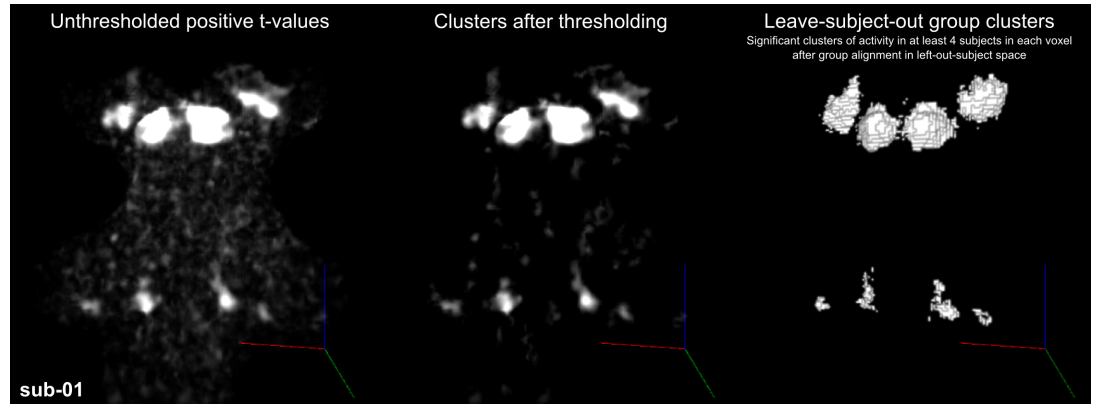


Figure 10. One frame of volume rendered animations for single subject statistical maps. (Left) positive t-values (middle) after thresholding (right) leave-one-out probabilistic map (≥ 4). Viewing angle here is similar to Figure 1.

- Figure 10-video 1.** Subject 01
- Figure 10-video 2.** Subject 02
- Figure 10-video 3.** Subject 03
- Figure 10-video 4.** Subject 05
- Figure 10-video 5.** Subject 06
- Figure 10-video 6.** Subject 07
- Figure 10-video 7.** Subject 08
- Figure 10-video 8.** Subject 09
- Figure 10-video 9.** Subject 10
- Figure 10-video 10.** Subject 11

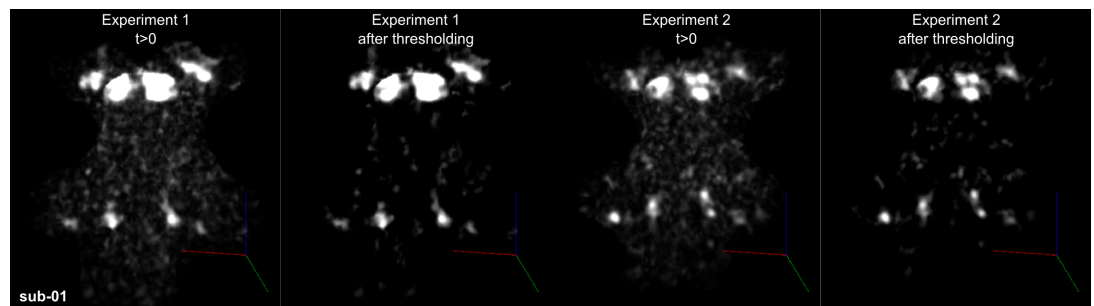


Figure 11. One frame of volume rendered animations for Subject 01 statistical maps (experiment 1 positive t-values & thresholded (col 1-2) and experiment 2 positive t-values & thresholded (col 3-4)). Viewing angle here is similar to Figure 1.

- Figure 11-video 1.** Subject 01 experiment 1 vs experiment 2.
- Figure 11-video 2.** Subject 02 experiment 1 vs experiment 2.
- Figure 11-video 3.** Subject 05 experiment 1 vs experiment 2.
- Figure 11-video 4.** Subject 09 experiment 1 vs experiment 2.
- Figure 11-video 5.** Subject 10 experiment 1 vs experiment 2.
- Figure 11-video 6.** Subject 11 experiment 1 vs experiment 2.
- Figure 11-video 7.** Group average (N=6) unthresholded positive t-values for experiment 1 vs experiment 2.

988 **Glossary**989 **Anatomical abbreviations**

AVCN	Anteroventral cochlear nucleus.
CN	Cochlear nucleus.
CNVIII	8th nerve, vestibulocochlear nerve.
DCN	Dorsal cochlear nucleus.
IC	Inferior colliculus.
LGN	Lateral geniculate nucleus.
990 LSO	Lateral superior olive.
MGB/MGN	Medial geniculate body/nucleus.
MNTB	Medial nucleus of the trapezoid body.
MSO	Medial superior olive.
PVCN	Posteroventral cochlear nucleus.
SOC	Superior olivary complex.

991 **MRI acquisition abbreviations**

7T	7 Tesla.
dMRI	diffusion magnetic resonance imaging.
FOV	Field of view.
fMRI	functional magnetic resonance imaging.
GRAPPA	Generalized auto-calibrating partially parallel acquisitions.
MB	Multi-band.
MPRAGE	Magnetization prepared rapid acquisition gradient echo.
992 MRI	Magnetic resonance imaging.
PDw	Proton density weighted.
SI-T1w	Short inversion time T1-weighted.
T1w	T1-weighted.
T2*w	T2*-weighted.
TE	Echo time.
TR	Repetition time.

993 **Data analysis abbreviations**

CSD	Constrained spherical deconvolution.
FA	Fractional anisotropy.
FDR	False discovery rate.
FOD	Fiber orientation distribution.
GLM	General linear model.
HCP	Human connectome project.
HRF	Hemodynamic response function.
994 ICBM	International Consortium for Brain Mapping.
MO	T2 signal with no diffusion weighting.
MD	Mean diffusivity.
MNI	Montreal Neurological Institute.
MSMT	Multi-shell multi-tissue
ODFs	Orientation distribution functions.
ROI	Region of interest.

References

- 995
996 **Amunts K**, Lepage C, Borgeat L, Mohlberg H, Dickscheid T, Rousseau MÉ, Bludau S, Bazin PL, Lewis LB, Oros-
997 Peusquens AM, Shah NJ, Lippert T, Zilles K, Evans AC. BigBrain: An ultrahigh-resolution 3D human brain
998 model. *Science*. 2013; doi: [10.1126/science.1235381](https://doi.org/10.1126/science.1235381).
- 999 **Amunts K**, Morosan P, Hilbig H, Zilles K. Auditory system. In: *The Human Nervous System* Elsevier; 2012.p.
1000 1270–1300.
- 1001 **Andersson JLR**, Jenkinson M, Smith S. Non-linear registration, aka spatial normalisation. FMRIB Technial Report
1002 TR07JA2.; 2007.
- 1003 **Andersson JLR**, Skare S, Ashburner J. How to correct susceptibility distortions in spin-echo echo-planar
1004 images: application to diffusion tensor imaging. *NeuroImage*. 2003 oct; 20(2):870–88. doi: [10.1016/S1053-](https://doi.org/10.1016/S1053-8119(03)00336-7)
1005 [8119\(03\)00336-7](https://doi.org/10.1016/S1053-8119(03)00336-7).
- 1006 **Andersson JLR**, Sotiropoulos SN. Non-parametric representation and prediction of single- and multi-
1007 shell diffusion-weighted MRI data using Gaussian processes. *NeuroImage*. 2015 nov; 122:166–76. doi:
1008 [10.1016/j.neuroimage.2015.07.067](https://doi.org/10.1016/j.neuroimage.2015.07.067).
- 1009 **Andersson JLR**, Sotiropoulos SN. An integrated approach to correction for off-resonance effects
1010 and subject movement in diffusion MR imaging. *NeuroImage*. 2016 jan; 125:1063–1078. doi:
1011 [10.1016/j.neuroimage.2015.10.019](https://doi.org/10.1016/j.neuroimage.2015.10.019).
- 1012 **Ashburner J**, Friston KJ. Unified segmentation. *NeuroImage*. 2005 jul; 26(3):839–851. doi:
1013 [10.1016/j.neuroimage.2005.02.018](https://doi.org/10.1016/j.neuroimage.2005.02.018).
- 1014 **Avants BB**, Tustison NJ, Song G, Cook PA, Klein A, Gee JC. A reproducible evaluation of ANTs similarity metric
1015 performance in brain image registration. *NeuroImage*. 2011 feb; 54(3):2033–44. [http://www.ncbi.nlm.](http://www.ncbi.nlm.nih.gov/pubmed/20851191)
1016 [nih.gov/pubmed/20851191](http://www.ncbi.nlm.nih.gov/pubmed/20851191)<http://www.pubmedcentral.nih.gov/articlerender.fcgi?artid=PMC3065962>, doi:
1017 [10.1016/j.neuroimage.2010.09.025](https://doi.org/10.1016/j.neuroimage.2010.09.025).
- 1018 **Behrens TEJ**, Berg HJ, Jbabdi S, Rushworth MFS, Woolrich MW. Probabilistic diffusion tractography with multiple
1019 fibre orientations: What can we gain? *NeuroImage*. 2007 jan; 34(1):144–55. [http://www.ncbi.nlm.nih.gov/](http://www.ncbi.nlm.nih.gov/pubmed/17070705)
1020 [pubmed/17070705](http://www.ncbi.nlm.nih.gov/pubmed/17070705), doi: [10.1016/j.neuroimage.2006.09.018](https://doi.org/10.1016/j.neuroimage.2006.09.018).
- 1021 **Brett M**, Hanke M, Côté MA, Markiewicz C, Ghosh S, Wassermann D, Gerhard S, Larson E, Lee GR, Halchenko Y,
1022 Kastman E, M C, Morency FC, Maloney B, Rokem A, Cottaar M, Millman J, jaeilepp, Gramfort A, Vincent RD,
1023 et al. nipy/nibabel: 2.2.0. . 2017 Oct; <https://doi.org/10.5281/zenodo.1011207>, doi: [10.5281/zenodo.1011207](https://doi.org/10.5281/zenodo.1011207).
- 1024 **Calabrese E**, Hickey P, Hulette C, Zhang J, Parente B, Lad SP, Johnson GA. Postmortem diffusion MRI of the
1025 human brainstem and thalamus for deep brain stimulator electrode localization. *Human brain mapping*.
1026 2015 aug; 36(8):3167–78. <http://www.ncbi.nlm.nih.gov/pubmed/26043869>[http://www.pubmedcentral.nih.](http://www.pubmedcentral.nih.gov/articlerender.fcgi?artid=PMC4652933)
1027 [gov/articlerender.fcgi?artid=PMC4652933](http://www.ncbi.nlm.nih.gov/pubmed/26043869), doi: [10.1002/hbm.22836](https://doi.org/10.1002/hbm.22836).
- 1028 **De Martino F**, Moerel M, van de Moortele PF, Ugurbil K, Goebel R, Yacoub E, Formisano E. Spatial organization
1029 of frequency preference and selectivity in the human inferior colliculus. *Nature communications*. 2013;
1030 4:1386. <http://www.ncbi.nlm.nih.gov/pubmed/23340426>[http://www.pubmedcentral.nih.gov/articlerender.](http://www.pubmedcentral.nih.gov/articlerender.fcgi?artid=PMC3556928)
1031 [fcgi?artid=PMC3556928](http://www.ncbi.nlm.nih.gov/pubmed/23340426), doi: [10.1038/ncomms2379](https://doi.org/10.1038/ncomms2379).
- 1032 **De Martino F**, Moerel M, Xu J, van de Moortele PF, Ugurbil K, Goebel R, Yacoub E, Formisano E. High-Resolution
1033 Mapping of Myeloarchitecture In Vivo: Localization of Auditory Areas in the Human Brain. *Cerebral cortex*
1034 (New York, NY : 1991). 2015 oct; 25(10):3394–405. <http://www.ncbi.nlm.nih.gov/pubmed/24994817><http://www.pubmedcentral.nih.gov/articlerender.fcgi?artid=PMC4585494>, doi: [10.1093/cercor/bhu150](https://doi.org/10.1093/cercor/bhu150).
- 1036 **De No RL**. III. General Plan of Structure of the Primary Cochlear Nuclei. *The Laryngoscope*. 1933 apr; 43(4):327–
1037 349. <http://doi.wiley.com/10.1288/00005537-193304000-00014>, doi: [10.1288/00005537-193304000-00014](https://doi.org/10.1288/00005537-193304000-00014).
- 1038 **De No RL**. The central projection of the nerve endings of the internal ear. *The Laryngoscope*. 1933 jan; 43(1):1–38.
1039 <http://doi.wiley.com/10.1288/00005537-193301000-00001>, doi: [10.1288/00005537-193301000-00001](https://doi.org/10.1288/00005537-193301000-00001).
- 1040 **Devlin JT**, Sillery EL, Hall DA, Hobden P, Behrens TEJ, Nunes RG, Clare S, Matthews PM, Moore DR, Johansen-Berg
1041 H. Reliable identification of the auditory thalamus using multi-modal structural analyses. *NeuroImage*. 2006
1042 may; 30(4):1112–20. <http://www.ncbi.nlm.nih.gov/pubmed/16473021>[http://www.pubmedcentral.nih.gov/](http://www.pubmedcentral.nih.gov/articlerender.fcgi?artid=PMC1458525)
1043 [articlerender.fcgi?artid=PMC1458525](http://www.ncbi.nlm.nih.gov/pubmed/16473021), doi: [10.1016/j.neuroimage.2005.11.025](https://doi.org/10.1016/j.neuroimage.2005.11.025).

- 1044 **Dhollander T**, Raffelt D, Connelly A. Unsupervised 3-tissue response function estimation from single-shell or
 1045 multi-shell diffusion MR data without a co-registered T1 image. In: *ISMRM Workshop on Breaking the Barriers of*
 1046 *Diffusion MRI*; 2016. p. 5.
- 1047 **Dhollander T**, Raffelt D, Connelly A. Unsupervised 3-tissue response function estimation from single-shell or
 1048 multi-shell diffusion MR data without a co-registered T1 image. In: *Proceedings of the 26th annual meeting of*
 1049 *the International Society of Magnetic Resonance in Medicine*; 2018. p. 1569.
- 1050 **Ding SL**, Royall JJ, Sunkin SM, Ng L, Facer BAC, Lesnar P, Guillozet-Bongaarts A, McMurray B, Szafer A, Dolbeare
 1051 TA, Stevens A, Tirrell L, Benner T, Caldejon S, Dalley RA, Dee N, Lau C, Nyhus J, Reding M, Riley ZL, et al.
 1052 Comprehensive cellular-resolution atlas of the adult human brain. . 2016; doi: [10.1002/cne.24097](https://doi.org/10.1002/cne.24097).
- 1053 **Duvernoy HM**. Human Brain Stem Vessels: Including the Pineal Gland and Information on Brain Stem
 1054 Infarction, vol. 11. Springer Science & Business Media; 2013. [https://books.google.com/books?id=](https://books.google.com/books?id=K87sCAAQBAJ&pgis=1)
 1055 [K87sCAAQBAJ&pgis=1](https://books.google.com/books?id=K87sCAAQBAJ&pgis=1).
- 1056 **Evans EF**. Cochlear Nerve and Cochlear Nucleus. In: *Handbook of Sensory Physiology* Springer Berlin Heidelberg;
 1057 1975.p. 1–108. http://www.springerlink.com/index/10.1007/978-3-642-65995-9_1, doi: 10.1007/978-3-642-
 1058 65995-9_1.
- 1059 **Fonov V**, Evans AC, Botteron K, Almli CR, McKinstry RC, Collins DL. Unbiased average age-appropriate atlases
 1060 for pediatric studies. *NeuroImage*. 2011; 54(1):313–327. <http://dx.doi.org/10.1016/j.neuroimage.2010.07.033>,
 1061 doi: [10.1016/j.neuroimage.2010.07.033](https://doi.org/10.1016/j.neuroimage.2010.07.033).
- 1062 **Fonov V**, Evans A, McKinstry R, Almli C, Collins D. Unbiased nonlinear average age-appropriate brain tem-
 1063 plates from birth to adulthood. *NeuroImage*. 2009; 47:S102. [http://linkinghub.elsevier.com/retrieve/pii/](http://linkinghub.elsevier.com/retrieve/pii/S1053811909708845)
 1064 [S1053811909708845](http://linkinghub.elsevier.com/retrieve/pii/S1053811909708845), doi: 10.1016/S1053-8119(09)70884-5.
- 1065 **Friston KJ**, Holmes AP, Worsley KJ, Poline JP, Frith CD, Frackowiak RSJ. Statistical parametric maps in functional
 1066 imaging: A general linear approach. *Human Brain Mapping*. 1994; doi: [10.1002/hbm.460020402](https://doi.org/10.1002/hbm.460020402).
- 1067 **Garcia-Gomar MG**, Strong C, Toschi N, Singh K, Rosen BR, Wald LL, Bianciardi M. In vivo probabilistic structural
 1068 atlas of the inferior and superior colliculi, medial and lateral geniculate nuclei and superior olivary complex
 1069 based on 7 Tesla MRI. *Frontiers in Neuroscience*. 2019; 13:764.
- 1070 **Garyfallidis E**. Towards an accurate brain tractography. PhD thesis, University of Cambridge; 2013.
- 1071 **Garyfallidis E**, Brett M, Amirkhanyan B, Rokem A, van der Walt S, Descoteaux M, Nimmo-Smith I, Dipy Contrib-
 1072 utors. Dipy, a library for the analysis of diffusion MRI data. *Frontiers in neuroinformatics*. 2014; 8:8. doi:
 1073 [10.3389/fninf.2014.00008](https://doi.org/10.3389/fninf.2014.00008).
- 1074 **Glasser MF**, Coalson TS, Robinson EC, Hacker CD, Harwell J, Yacoub E, Ugurbil K, Andersson J, Beckmann CF,
 1075 Jenkinson M, Smith SM, Van Essen DC. A multi-modal parcellation of human cerebral cortex. *Nature*. 2016;
 1076 doi: [10.1038/nature18933](https://doi.org/10.1038/nature18933).
- 1077 **Glendenning KK**, Masterton RB. Comparative Morphometry of Mammalian Central Auditory Systems: Variation
 1078 in Nuclei and Form of the Ascending System. *Brain Behav Evol*. 1998; 51:59–89. [http://www.karger.chhttp://](http://www.karger.chhttp://biomednet.com/karger)
 1079 [biomednet.com/karger](http://www.karger.chhttp://biomednet.com/karger).
- 1080 **Goebel R**. BrainVoyager — Past, present, future. *NeuroImage*. 2012 aug; 62(2):748–756. doi:
 1081 [10.1016/j.neuroimage.2012.01.083](https://doi.org/10.1016/j.neuroimage.2012.01.083).
- 1082 **Gorgolewski K**, Burns CD, Madison C, Clark D, Halchenko YO, Waskom ML, Ghosh SS. Nipype: a flexible,
 1083 lightweight and extensible neuroimaging data processing framework in python. *Front Neuroinform*. 2011 08;
 1084 5. <https://doi.org/10.3389/fninf.2011.00013>, doi: [10.3389/fninf.2011.00013](https://doi.org/10.3389/fninf.2011.00013).
- 1085 **Gray H**, Lewis W. Anatomy of the human body. 20 ed. Philadelphia: Lea & Febiger; 1918.
- 1086 **Griffiths TD**, Uppenkamp S, Johnsrude I, Josephs O, Patterson RD. Encoding of the temporal regularity of sound
 1087 in the human brainstem. *Nature Neuroscience*. 2001; doi: [10.1038/88459](https://doi.org/10.1038/88459).
- 1088 **Griswold MA**, Jakob PM, Heidemann RM, Nittka M, Jellus V, Wang J, Kiefer B, Haase A. Generalized Autocalibrating
 1089 Partially Parallel Acquisitions (GRAPPA). *Magnetic Resonance in Medicine*. 2002; 47(6):1202–1210. doi:
 1090 [10.1002/mrm.10171](https://doi.org/10.1002/mrm.10171).

- 1091 **Guimaraes AR**, Melcher JR, Talavage TM, Baker JR, Ledden P, Rosen BR, Kiang NYS, Fullerton BC, Weisskoff RM.
1092 Imaging subcortical auditory activity in humans. *Human Brain Mapping*. 1998; 6(1):33–41. <http://doi.wiley.com/10.1002/{%}28SICI{%}291097-0193{%}281998{%}296{%}3A1{%}3C33{%}3A{%}3AAID-HBM3{%}3E3.0.CO{%}3B2-M>, doi: 10.1002/(SICI)1097-0193(1998)6:1<33::AID-HBM3>3.0.CO;2-M.
- 1095 **Gulban OF**, De Martino F, Vu AT, Yacoub E, Uğurbil K, Lenglet C. Cortical fibers orientation mapping using in-vivo
1096 whole brain 7 T diffusion MRI. *NeuroImage*. 2018 sep; 178(December 2017):104–118. <http://linkinghub.elsevier.com/retrieve/pii/S1053811918304087https://linkinghub.elsevier.com/retrieve/pii/S1053811918304087>, doi:
1097 [10.1016/j.neuroimage.2018.05.010](https://doi.org/10.1016/j.neuroimage.2018.05.010).
1098
- 1099 **Gulban OF**, Schneider M, Marquardt I, Haast RAM, De Martino F. A scalable method to improve gray matter
1100 segmentation at ultra high field MRI. *PLOS ONE*. 2018 jun; 13(6):e0198335. <http://dx.plos.org/10.1371/journal.pone.0198335>, doi: 10.1371/journal.pone.0198335.
1101
- 1102 **Harms MP**, Melcher JR. Sound repetition rate in the human auditory pathway: representations in the waveshape
1103 and amplitude of fMRI activation. *Journal of neurophysiology*. 2002 sep; 88(3):1433–50. <http://www.ncbi.nlm.nih.gov/pubmed/12205164>, doi: 10.1152/jn.2002.88.3.1433.
1104
- 1105 **Hawley ML**, Melcher JR, Fullerton BC. Effects of sound bandwidth on fMRI activation in human
1106 auditory brainstem nuclei. *Hearing research*. 2005 jun; 204(1-2):101–10. <http://www.ncbi.nlm.nih.gov/pubmed/15925195http://www.pubmedcentral.nih.gov/articlerender.fcgi?artid=PMC1855158>, doi:
1107 [10.1016/j.heares.2005.01.005](https://doi.org/10.1016/j.heares.2005.01.005).
1108
- 1109 **Hawrylycz MJ**, Lein ES, Guillozet-Bongaarts AL, Shen EH, Ng L, Miller JA, van de Lagemaat LN, Smith KA,
1110 Ebbert A, Riley ZL, Abajian C, Beckmann CF, Bernard A, Bertagnolli D, Boe AF, Cartagena PM, Chakravarty
1111 MM, Chapin M, Chong J, Dalley RA, et al. An anatomically comprehensive atlas of the adult human brain
1112 transcriptome. *Nature*. 2012 sep; 489(7416):391–399. <http://www.ncbi.nlm.nih.gov/pubmed/22996553http://www.pubmedcentral.nih.gov/articlerender.fcgi?artid=PMC4243026>, doi: 10.1038/nature11405.
1113
- 1114 **Javad F**, Warren JD, Micallef C, Thornton JS, Golay X, Yousry T, Mancini L. Auditory tracts identified with
1115 combined fMRI and diffusion tractography. *NeuroImage*. 2014 jan; 84:562–74. <http://www.ncbi.nlm.nih.gov/pubmed/24051357http://www.pubmedcentral.nih.gov/articlerender.fcgi?artid=PMC3898984>, doi:
1116 [10.1016/j.neuroimage.2013.09.007](https://doi.org/10.1016/j.neuroimage.2013.09.007).
1117
- 1118 **Jenkinson M**, Beckmann CF, Behrens TEJ, Woolrich MW, Smith SM. FSL. *NeuroImage*. 2012 aug; 62(2):782–790.
1119 doi: 10.1016/j.neuroimage.2011.09.015.
- 1120 **Jeurissen B**, Tournier JD, Dhollander T, Connelly A, Sijbers J. Multi-tissue constrained spherical deconvolution
1121 for improved analysis of multi-shell diffusion MRI data. *NeuroImage*. 2014 dec; 103:411–426. <http://www.ncbi.nlm.nih.gov/pubmed/25109526>, doi: 10.1016/j.neuroimage.2014.07.061.
1122
- 1123 **Jiang ZD**, Moore DR, J King A. Sources of subcortical projections to the superior colliculus in the ferret. *Brain*
1124 *Research*. 1997 may; 755(2):279–292. <http://linkinghub.elsevier.com/retrieve/pii/S0006899397001054>, doi:
1125 [10.1016/S0006-8993\(97\)00105-4](https://doi.org/10.1016/S0006-8993(97)00105-4).
- 1126 **Johnson GA**, Benveniste H, Black RD, Hedlund LW, Maronpot RR, Smith BR. Histology by magnetic resonance
1127 microscopy. *Magnetic resonance quarterly*. 1993 mar; 9(1):1–30. <http://www.ncbi.nlm.nih.gov/pubmed/8512830>, doi: 10.1139/m63-008.
1128
- 1129 **Kay KN**, Rokem A, Winawer J, Dougherty RF, Wandell BA. GLMdenoise: A fast, automated technique for denoising
1130 task-based fMRI data. *Frontiers in Neuroscience*. 2013; doi: 10.3389/fnins.2013.00247.
- 1131 **Kulesza RJ**. Cytoarchitecture of the human superior olivary complex: medial and lateral superior
1132 olive. *Hearing research*. 2007 mar; 225(1-2):80–90. <http://www.ncbi.nlm.nih.gov/pubmed/17250984>, doi:
1133 [10.1016/j.heares.2006.12.006](https://doi.org/10.1016/j.heares.2006.12.006).
- 1134 **Kulesza RJ**, Grothe B. Yes, there is a medial nucleus of the trapezoid body in humans. *Frontiers in*
1135 *neuroanatomy*. 2015 may; 9(5):35. <http://www.ncbi.nlm.nih.gov/pubmed/4379933http://www.ncbi.nlm.nih.gov/pubmed/25873865http://www.pubmedcentral.nih.gov/articlerender.fcgi?artid=PMC4379933>, doi:
1136 [10.3389/fnana.2015.00035](https://doi.org/10.3389/fnana.2015.00035).
1137
- 1138 **Lévy B**. A Numerical Algorithm for L 2 Semi-Discrete Optimal Transport in 3D. *ESAIM: Mathematical Modelling*
1139 *and Numerical Analysis*. 2015 nov; 49(6):1693–1715. <http://www.esaim-m2an.org/10.1051/m2an/2015055>,
1140 doi: 10.1051/m2an/2015055.

- 1141 **Lévy B**, Schwindt EL. Notions of optimal transport theory and how to implement them on a computer.
1142 Computers and Graphics (Pergamon). 2018; doi: [10.1016/j.cag.2018.01.009](https://doi.org/10.1016/j.cag.2018.01.009).
- 1143 **Maffei C**, Jovicich J, De Benedictis A, Corsini F, Barbareschi M, Chioffi F, Sarubbo S. Topography of the human
1144 acoustic radiation as revealed by ex vivo fibers micro-dissection and in vivo diffusion-based tractography.
1145 Brain structure & function. 2018 jan; 223(1):449–459. <http://www.ncbi.nlm.nih.gov/pubmed/28866840>, doi:
1146 10.1007/s00429-017-1471-6.
- 1147 **Malmierca MS**, Hackett TA. Structural organization of the ascending auditory pathway. The Auditory Brain.
1148 2010; p. 9–41.
- 1149 **Merker B**. Silver staining of cell bodies by means of physical development. Journal of Neuroscience Methods.
1150 1983 nov; 9(3):235–241. <http://linkinghub.elsevier.com/retrieve/pii/0165027083900869>, doi: 10.1016/0165-
1151 0270(83)90086-9.
- 1152 **Miller KL**, Stagg CJ, Douaud G, Jbabdi S, Smith SM, Behrens TEJ, Jenkinson M, Chance SA, Esiri MM, Voets NL,
1153 Jenkinson N, Aziz TZ, Turner MR, Johansen-Berg H, McNab JA. Diffusion imaging of whole, post-mortem
1154 human brains on a clinical MRI scanner. NeuroImage. 2011 jul; 57(1):167–181. [http://www.pubmedcentral.
1155 nih.gov/articlerender.fcgi?artid=PMC3115068](http://www.pubmedcentral.nih.gov/articlerender.fcgi?artid=PMC3115068), doi: 10.1016/j.neuroimage.2011.03.070.
- 1156 **Moeller S**, Yacoub E, Olman CA, Auerbach E, Strupp J, Harel N, Uğurbil K. Multiband multislice GE-EPI at 7 tesla,
1157 with 16-fold acceleration using partial parallel imaging with application to high spatial and temporal whole-
1158 brain fMRI. Magnetic resonance in medicine. 2010 may; 63(5):1144–53. [http://www.ncbi.nlm.nih.gov/pubmed/
1159 20432285](http://www.ncbi.nlm.nih.gov/pubmed/20432285)<http://www.pubmedcentral.nih.gov/articlerender.fcgi?artid=PMC2906244>, doi: 10.1002/mrm.22361.
- 1160 **Moerel M**, De Martino F, Uğurbil K, Yacoub E, Formisano E. Processing of frequency and location in human
1161 subcortical auditory structures. Scientific reports. 2015 nov; 5:17048. doi: 10.1038/srep17048.
- 1162 **Moore JK**. The human auditory brain stem: a comparative view. Hearing research. 1987; 29:1–32. doi:
1163 10.1016/0378-5955(87)90202-4.
- 1164 **Moore JK**, Perazzo LM, Braun A. Time course of axonal myelination in the human brainstem auditory pathway.
1165 Hearing research. 1995 jul; 87(1-2):21–31. <http://www.ncbi.nlm.nih.gov/pubmed/8567438>, doi: 10.1016/0378-
1166 5955(95)00218-9.
- 1167 **Mori S**, Crain BJ, Chacko VP, van Zijl PC. Three-dimensional tracking of axonal projections in the brain by
1168 magnetic resonance imaging. Annals of neurology. 1999 feb; 45(2):265–9. [http://www.ncbi.nlm.nih.gov/
1169 pubmed/9989633](http://www.ncbi.nlm.nih.gov/pubmed/9989633), doi: 10.1002/1531-8249(199902)45:2<265::AID-ANA21>3.0.CO;2-3.
- 1170 **Paxinos G**, T F, C W. Human Brainstem: Cytoarchitecture, Chemoarchitecture, Myeloarchitecture. 1 ed. Academic
1171 Press; 2019.
- 1172 **Pfefferbaum A**, Sullivan EV, Adalsteinsson E, Garrick T, Harper C. Postmortem MR imaging of formalin-fixed
1173 human brain. NeuroImage. 2004 apr; 21(4):1585–95. <http://www.ncbi.nlm.nih.gov/pubmed/15050582>, doi:
1174 10.1016/j.neuroimage.2003.11.024.
- 1175 **Reveley C**, Seth AK, Pierpaoli C, Silva AC, Yu D, Saunders RC, Leopold DA, Ye FQ. Superficial white matter fiber
1176 systems impede detection of long-range cortical connections in diffusion MR tractography. Proceedings of the
1177 National Academy of Sciences of the United States of America. 2015 may; 112(21):E2820–8. [http://www.ncbi.
1178 nlm.nih.gov/pubmed/25964365](http://www.ncbi.nlm.nih.gov/pubmed/25964365)<http://www.pubmedcentral.nih.gov/articlerender.fcgi?artid=PMC4450402>, doi:
1179 10.1073/pnas.1418198112.
- 1180 **Rose J**, Galambos R, Hughes J. Organization of frequency sensitive neurons in the cochlear nuclear complex
1181 of the cat. In: *Neural Mechanisms of the Auditory and Vestibular Systems* Thomas Springfield, IL; 1960.p.
1182 116–136. [#0](http://scholar.google.com/scholar?hl=en&btnG=Search&q=intitle:Organization+of+frequency+sensitive+neurons+in+the+cochlear+nuclear+complex+of+the+cat).
1183 [#0](http://scholar.google.com/scholar?hl=en&btnG=Search&q=intitle:Organization+of+frequency+sensitive+neurons+in+the+cochlear+nuclear+complex+of+the+cat).
- 1184 **Ryugo DK**, May SK. The projections of intracellularly labeled auditory nerve fibers to the dorsal cochlear nucleus
1185 of cats. The Journal of comparative neurology. 1993 mar; 329(1):20–35. [http://www.ncbi.nlm.nih.gov/pubmed/
1186 8454724](http://www.ncbi.nlm.nih.gov/pubmed/8454724), doi: 10.1002/cne.903290103.
- 1187 **Ryugo DK**, Parks TN. Primary innervation of the avian and mammalian cochlear nucleus. Brain Research
1188 Bulletin. 2003; 60(5-6):435–456. doi: 10.1016/S0361-9230(03)00049-2.
- 1189 **Sando I**. The Anatomical Interrelationships of the Cochlear Nerve Fibers. Acta Oto-Laryngologica.
1190 1965 jan; 59(2-6):417–436. <http://www.tandfonline.com/doi/full/10.3109/00016486509124577>, doi:
1191 10.3109/00016486509124577.

- 1192 **Schilling KG**, Daducci A, Maier-Hein K, Poupon C, Houde JC, Nath V, Anderson AW, Landman BA, Descoteaux
1193 M. Challenges in diffusion MRI tractography - Lessons learned from international benchmark competitions.
1194 Magnetic resonance imaging. 2019 apr; 57:194–209. <http://www.ncbi.nlm.nih.gov/pubmed/30503948>
1195 <http://www.pubmedcentral.nih.gov/articlerender.fcgi?artid=PMC6331218>, doi: 10.1016/j.mri.2018.11.014.
- 1196 **Schilling KG**, Nath V, Hansen C, Parvathaneni P, Blaber J, Gao Y, Neher P, Aydogan DB, Shi Y, Ocampo-Pineda M,
1197 Schiavi S, Daducci A, Girard G, Barakovic M, Rafael-Patino J, Romascano D, Rensonnet G, Pizzolato M, Bates A,
1198 Fisci E, et al. Limits to anatomical accuracy of diffusion tractography using modern approaches. NeuroImage.
1199 2019; doi: 10.1016/j.neuroimage.2018.10.029.
- 1200 **Schofield BR**. Structural organization of the descending auditory pathway. The Auditory Brain. 2010; p. 43–64.
- 1201 **Setsonpop K**, Gagoski BA, Polimeni JR, Witzel T, Wedeen VJ, Wald LL. Blipped-controlled aliasing in par-
1202 allel imaging for simultaneous multislice echo planar imaging with reduced g-factor penalty. Magnetic
1203 resonance in medicine. 2012 may; 67(5):1210–24. <http://www.ncbi.nlm.nih.gov/pubmed/21858868>
1204 <http://www.pubmedcentral.nih.gov/articlerender.fcgi?artid=PMC3323676>, doi: 10.1002/mrm.23097.
- 1205 **Sigalovsky IS**, Melcher JR. Effects of sound level on fMRI activation in human brainstem, thalamic and cortical
1206 centers. Hearing research. 2006 may; 215(1-2):67–76. <http://www.ncbi.nlm.nih.gov/pubmed/16644153>
1207 <http://www.pubmedcentral.nih.gov/articlerender.fcgi?artid=PMC1794213>, doi: 10.1016/j.heares.2006.03.002.
- 1208 **Sitek KR**, Gulban OF, subcortical-auditory-atlas. GitHub; 2019. [https://github.com/sitek/](https://github.com/sitek/subcortical-auditory-atlas)
1209 [subcortical-auditory-atlas](https://github.com/sitek/subcortical-auditory-atlas).
- 1210 **Sotiropoulos SN**, Jbabdi S, Xu J, Andersson JL, Moeller S, Auerbach EJ, Glasser MF, Hernandez M, Sapiro
1211 G, Jenkinson M, Feinberg DA, Yacoub E, Lenglet C, Van Essen DC, Ugurbil K, Behrens TEJ. Advances in
1212 diffusion MRI acquisition and processing in the Human Connectome Project. NeuroImage. 2013; doi:
1213 10.1016/j.neuroimage.2013.05.057.
- 1214 **Sparks DL**, Hartwich-Young R. The deep layers of the superior colliculus. Reviews of oculomotor research. 1989;
1215 3:213–55. <http://www.ncbi.nlm.nih.gov/pubmed/2486324>.
- 1216 **Strominger NL**, Hurwitz JL. Anatomical aspects of the superior olivary complex. The Journal of comparative neuro-
1217 rology. 1976 dec; 170(4):485–97. <http://www.ncbi.nlm.nih.gov/pubmed/826550>, doi: 10.1002/cne.901700407.
- 1218 **Teeuwisse WM**, Brink WM, Webb AG. Quantitative assessment of the effects of high-permittivity pads in 7 tesla
1219 MRI of the brain. Magnetic resonance in medicine. 2012; 67(5):1285–1293.
- 1220 **Thomas C**, Ye FQ, Irfanoglu MO, Modi P, Saleem KS, Leopold DA, Pierpaoli C. Anatomical accuracy of brain con-
1221 nections derived from diffusion MRI tractography is inherently limited. Proceedings of the National Academy
1222 of Sciences. 2014 nov; 111(46):16574–16579. <http://www.pnas.org/lookup/doi/10.1073/pnas.1405672111>,
1223 doi: 10.1073/pnas.1405672111.
- 1224 **Tourdias T**, Saranathan M, Levesque IR, Su J, Rutt BK. Visualization of intra-thalamic nuclei with opti-
1225 mized white-matter-nulled MPRAGE at 7T. NeuroImage. 2014 jan; 84:534–45. [http://www.ncbi.nlm.](http://www.ncbi.nlm.nih.gov/pubmed/24018302)
1226 [nih.gov/pubmed/24018302](http://www.pubmedcentral.nih.gov/articlerender.fcgi?artid=PMC3927795)<http://www.pubmedcentral.nih.gov/articlerender.fcgi?artid=PMC3927795>, doi:
1227 10.1016/j.neuroimage.2013.08.069.
- 1228 **Tournier JD**, Calamante F, Connelly A. Robust determination of the fibre orientation distribution in diffu-
1229 sion MRI: Non-negativity constrained super-resolved spherical deconvolution. NeuroImage. 2007; doi:
1230 10.1016/j.neuroimage.2007.02.016.
- 1231 **Tournier JD**, Calamante F, Gadian DG, Connelly A. Direct estimation of the fiber orientation density
1232 function from diffusion-weighted MRI data using spherical deconvolution. NeuroImage. 2004; doi:
1233 10.1016/j.neuroimage.2004.07.037.
- 1234 **Triantafyllou C**, Polimeni JR, Keil B, Wald LL. Coil-to-coil physiological noise correlations and their impact on
1235 functional MRI time-series signal-to-noise ratio. Magnetic Resonance in Medicine. 2016 dec; 76(6):1708–1719.
1236 <http://doi.wiley.com/10.1002/mrm.26041>, doi: 10.1002/mrm.26041.
- 1237 **Ugurbil K**. What is feasible with imaging human brain function and connectivity using functional mag-
1238 netic resonance imaging. Philosophical Transactions of the Royal Society B: Biological Sciences. 2016
1239 oct; 371(1705):20150361. <http://rstb.royalsocietypublishing.org/lookup/doi/10.1098/rstb.2015.0361>, doi:
1240 10.1098/rstb.2015.0361.

- 1241 **Ugurbil K**, Adriany G, Andersen P, Chen W, Garwood M, Gruetter R, Henry PG, Kim SG, Lieu H, Tkac I, Vaughan
1242 T, Van De Moortele PF, Yacoub E, Zhu XH. Ultrahigh field magnetic resonance imaging and spectroscopy.
1243 *Magnetic Resonance Imaging*. 2003 dec; 21(10):1263–1281. [https://linkinghub.elsevier.com/retrieve/pii/](https://linkinghub.elsevier.com/retrieve/pii/S0730725X03003382)
1244 [S0730725X03003382](https://linkinghub.elsevier.com/retrieve/pii/S0730725X03003382), doi: 10.1016/j.mri.2003.08.027.
- 1245 **Van de Moortele PF**, Auerbach EJ, Olman C, Yacoub E, Ugurbil K, Moeller S. T1 weighted brain images at 7
1246 Tesla unbiased for Proton Density, T2* contrast and RF coil receive B1 sensitivity with simultaneous vessel
1247 visualization. *NeuroImage*. 2009 jun; 46(2):432–46. doi: 10.1016/j.neuroimage.2009.02.009.
- 1248 **Van Der Walt S**, Colbert SC, Varoquaux G. The NumPy array: a structure for efficient numerical computation.
1249 *Computing in Science & Engineering*. 2011; 13(2):22–30.
- 1250 **Vaughan JT**, Garwood M, Collins CM, Liu W, DelaBarre L, Adriany G, Andersen P, Merkle H, Goebel R, Smith
1251 MB, Ugurbil K. 7T vs. 4T: RF power, homogeneity, and signal-to-noise comparison in head images. *Mag-*
1252 *netic resonance in medicine*. 2001 jul; 46(1):24–30. <http://www.ncbi.nlm.nih.gov/pubmed/11443707>, doi:
1253 [10.1002/mrm.1156](https://doi.org/10.1002/mrm.1156).
- 1254 **Vu AT**, Auerbach E, Lenglet C, Moeller S, Sotiropoulos SN, Jbabdi S, Andersson J, Yacoub E, Ugurbil K. High
1255 resolution whole brain diffusion imaging at 7T for the Human Connectome Project. *NeuroImage*. 2015; doi:
1256 [10.1016/j.neuroimage.2015.08.004](https://doi.org/10.1016/j.neuroimage.2015.08.004).
- 1257 **Wallace MN**, Cronin MJ, Bowtell RW, Scott IS, Palmer AR, Gowland PA. Histological Basis of Laminar MRI
1258 Patterns in High Resolution Images of Fixed Human Auditory Cortex. *Frontiers in neuroscience*. 2016 oct;
1259 10:455. <http://www.ncbi.nlm.nih.gov/pubmed/27774049>[http://www.pubmedcentral.nih.gov/articlerender.](http://www.pubmedcentral.nih.gov/articlerender.fcgi?artid=PMC5054214)
1260 [fcgi?artid=PMC5054214](http://www.pubmedcentral.nih.gov/articlerender.fcgi?artid=PMC5054214), doi: 10.3389/fnins.2016.00455.
- 1261 **Wang N**, Anderson RJ, Badea A, Cofer G, Dibb R, Qi Y, Johnson GA. Whole mouse brain structural connectomics
1262 using magnetic resonance histology. *Brain structure & function*. 2018 dec; 223(9):4323–4335. [http://www.](http://www.ncbi.nlm.nih.gov/pubmed/30225830)
1263 [ncbi.nlm.nih.gov/pubmed/30225830](http://www.ncbi.nlm.nih.gov/pubmed/30225830), doi: 10.1007/s00429-018-1750-x.
- 1264 **Wang R**, Benner T, Sorensen AG, Wedeen VJ. Diffusion toolkit: a software package for diffusion imaging data
1265 processing and tractography. In: *Proc Intl Soc Mag Reson Med* Berlin; 2007. p. 3720.
- 1266 **Webster DB**. An Overview of Mammalian Auditory Pathways with an Emphasis on Humans. In: *Handbook*
1267 *of Auditory Research* Springer; 1992.p. 1–22. http://link.springer.com/10.1007/978-1-4612-4416-5_1, doi:
1268 [10.1007/978-1-4612-4416-5_1](https://doi.org/10.1007/978-1-4612-4416-5_1).
- 1269 **Winer Ja**. The human medial geniculate body. *Hearing Research*. 1984; 15(3):225–247. doi: 10.1016/0378-
1270 5955(84)90031-5.
- 1271 **Yushkevich PA**, Piven J, Hazlett HC, Smith RG, Ho S, Gee JC, Gerig G. User-guided 3D active contour segmentation
1272 of anatomical structures: significantly improved efficiency and reliability. *NeuroImage*. 2006 jul; 31(3):1116–28.
1273 doi: 10.1016/j.neuroimage.2006.01.015.
- 1274 **Zanin J**, Dhollander T, Farquharson S, Rance G, Connelly A, Nayagam BA. Review: Using diffusion-weighted
1275 magnetic resonance imaging techniques to explore the microstructure and connectivity of subcorti-
1276 cal white matter tracts in the human auditory system. *Hearing Research*. 2019 jun; 377:1–11. doi:
1277 [10.1016/j.heares.2019.02.014](https://doi.org/10.1016/j.heares.2019.02.014).

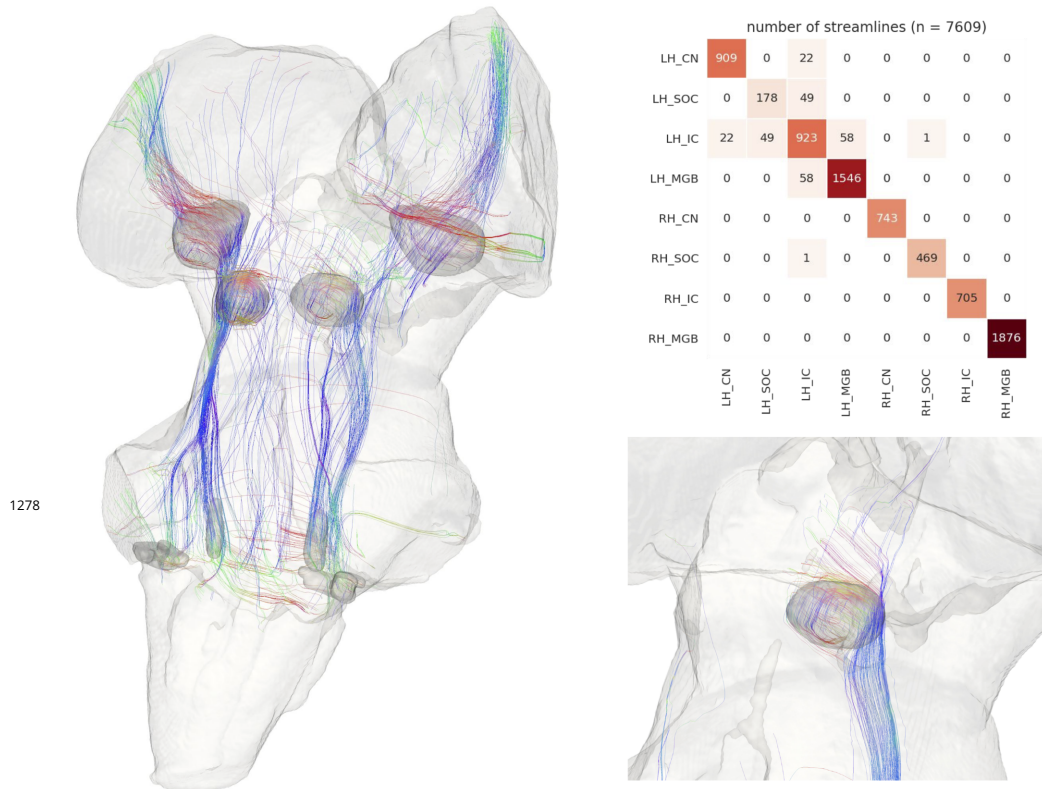


Figure 3-Figure supplement 1. Post mortem human diffusion-weighted MRI tractography (from 200 μm isotropic voxels) with anatomically defined subcortical auditory seeds, downsampled to 200 μm but undilated. Streamlines that passed through manual segmentations of the medulla and optic tracts were excluded. 10 percent of streamlines are visualized for clarity. Top right: connectivity heatmap of subcortical auditory structures. Bottom right: Streamlines that pass through the right inferior colliculus.

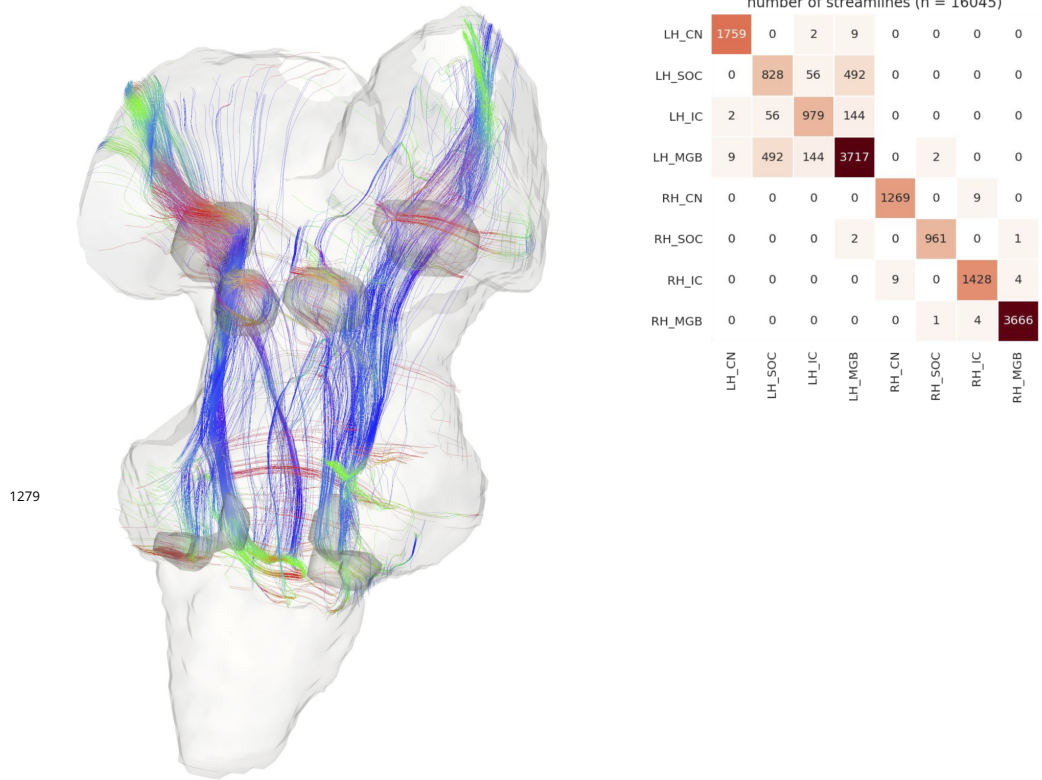


Figure 3–Figure supplement 2. Post mortem human diffusion-weighted MRI tractography with anatomically defined subcortical auditory seeds. MRI data were downsampled from 200 μm to 1050 μm to match in vivo data acquisition and then processed in the same manner as other diffusion tractography analyses. Streamlines that passed through manual segmentations of the medulla and optic tracts were excluded. 10 percent of streamlines are visualized for clarity. Top right: Connectivity heatmap of subcortical auditory structures.

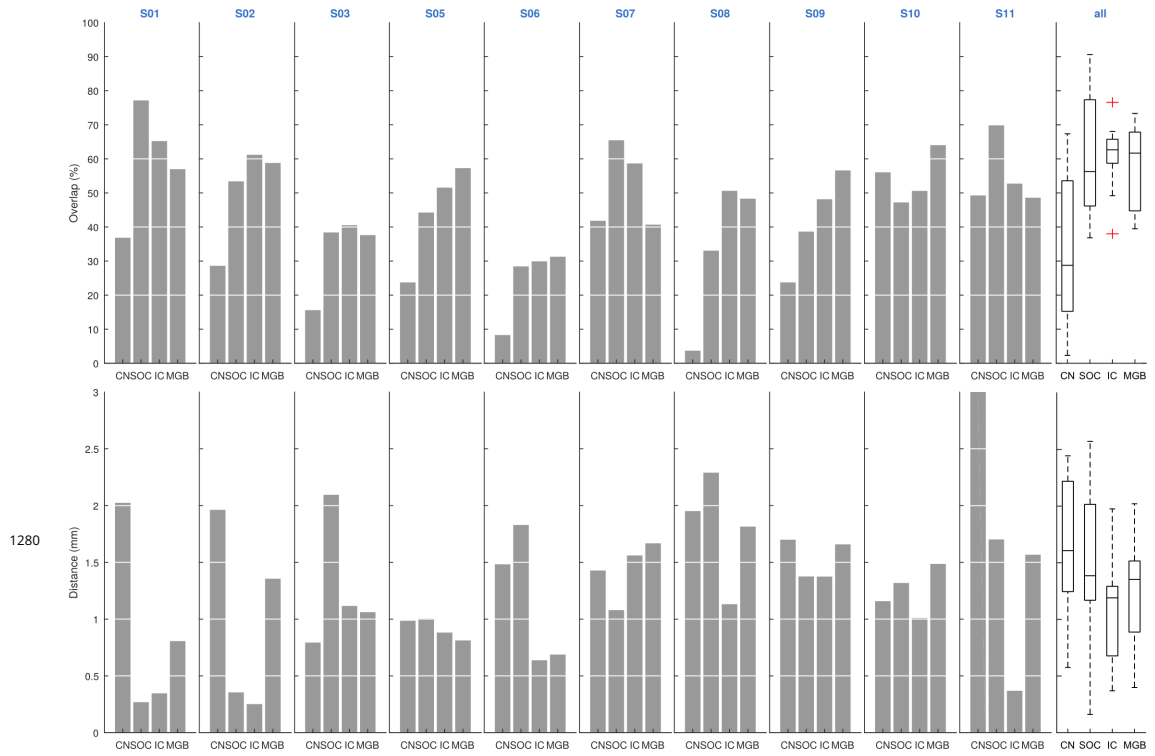


Figure 4-Figure supplement 1. Correspondence between single subject activation maps and leave-one-out functional probabilistic maps. Leave-one-out probabilistic functional maps are thresholded to identify voxels that are significantly responding to sounds in at least three of nine participants. The overlap represents (per region of interest) the percentage of the voxels on the leave-one-out probabilistic maps that is significantly responding to sounds in the left out subject. For each region of interest we also report the distance in mm between the centroids of the leave-one-out probabilistic maps and the centroids of the regions significantly responding to sounds in the left out subject. The last column represents the average overlap and distance across participants per region and error bars represent the standard error across the participants.

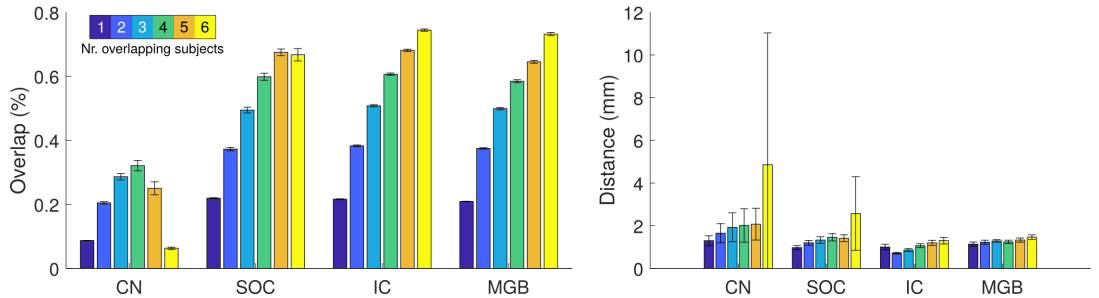


Figure 4-Figure supplement 2. Correspondence between single subject activation maps and leave-one-out functional probabilistic maps at different thresholds. Leave-one-out probabilistic functional maps are thresholded to identify voxels that are significantly responding to sounds by varying thresholds from at least one of nine participants to at least six of nine participants. The overlap represents (per region of interest) the percentage of the voxels on the leave-one-out probabilistic maps that is significantly responding to sounds in the left out subject. For each region of interest we also report the distance in mm between the centroids of the leave-one-out probabilistic maps and the centroids of the regions significantly responding to sounds in the left out subject. Boxplots represent the average overlap and distance across participants per region and error bars represent the standard error across the participants.

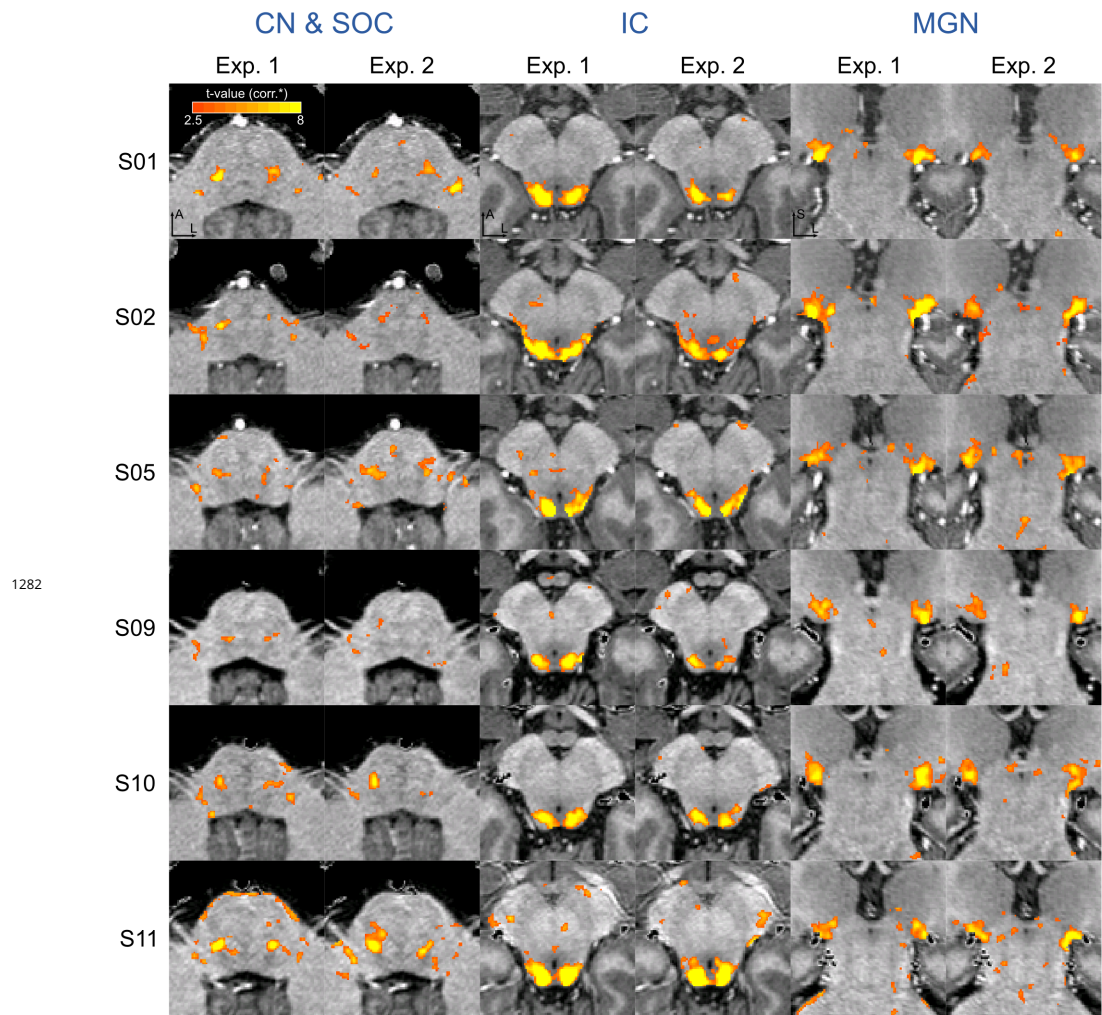


Figure 4-Figure supplement 3. Reproducibility of functional activation maps. Functional activation maps obtained from Experiment 1 and Experiment 2 (six participants) thresholded for significance (FDR- $q = 0.05$ and $p < 0.001$; see Methods for details). For each participant, CN/SOC and IC are shown in transversal cuts, MGB is shown in a coronal cut.

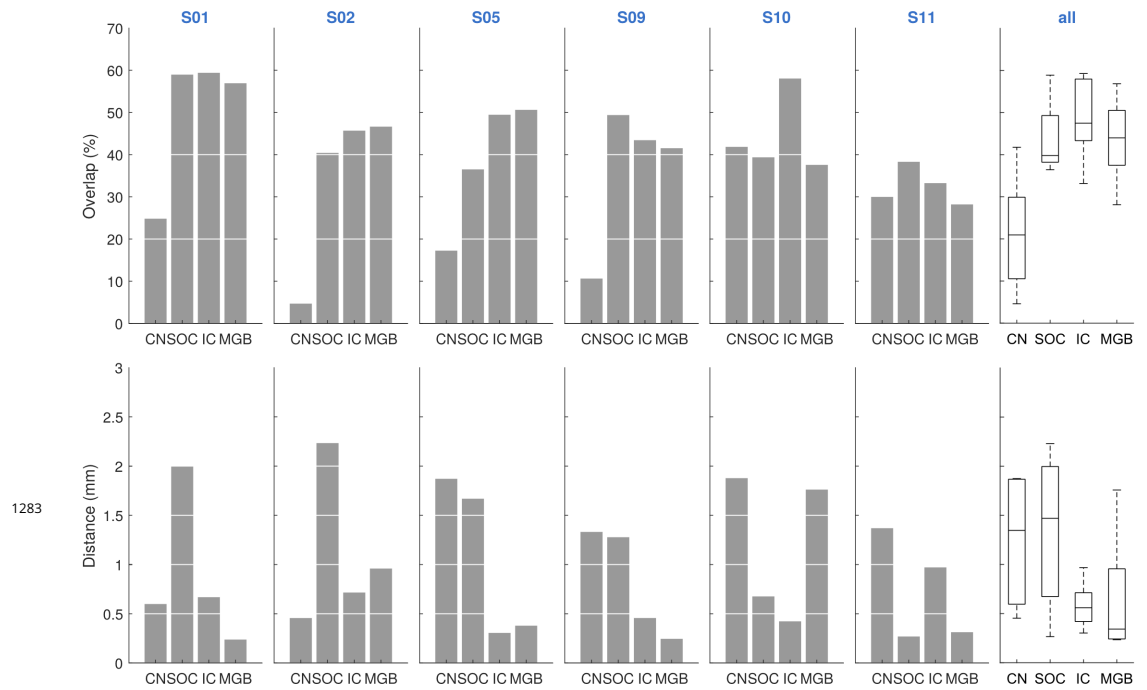


Figure 4-Figure supplement 4. Correspondence between single subject activation maps Experiment 1 and Experiment 2. All maps are thresholded for significance (FDR-q=0.05 and $p < 0.001$; see methods for details). The overlap represents (per region of interest) the percentage of the voxels significantly active in Experiment 1 that is significantly responding to sounds in Experiment 2. For each region of interest we also report the distance in mm between the centroids of the regions significantly responding to sounds in both experiments. Videos are provided in the appendix that visualize thresholded and unthresholded maps for each of the individual participants. The last column represents the average overlap and distance across participants per region and error bars represent the standard error across the participants.

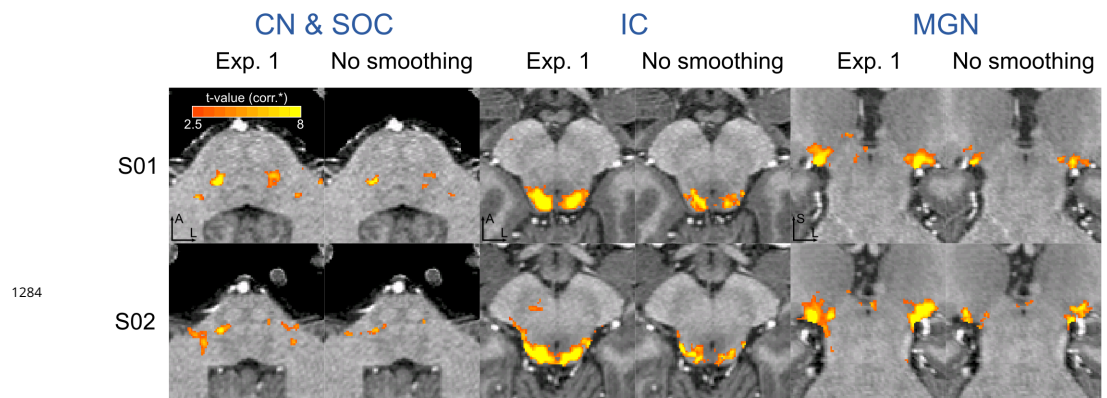


Figure 4-Figure supplement 5. Effect of spatial smoothing on functional activation maps. Functional activation maps obtained from Experiment 1 in two participants with and without applying spatial smoothing (1.5mm FWHM Gaussian smoothing) prior to the statistical analysis. Maps are thresholded for statistical significance (FDR-q = 0.05 & $p < 0.001$; see Methods for details). For each participant, CN/SOC and IC are shown in transversal cuts, MGN is shown in a coronal cut.

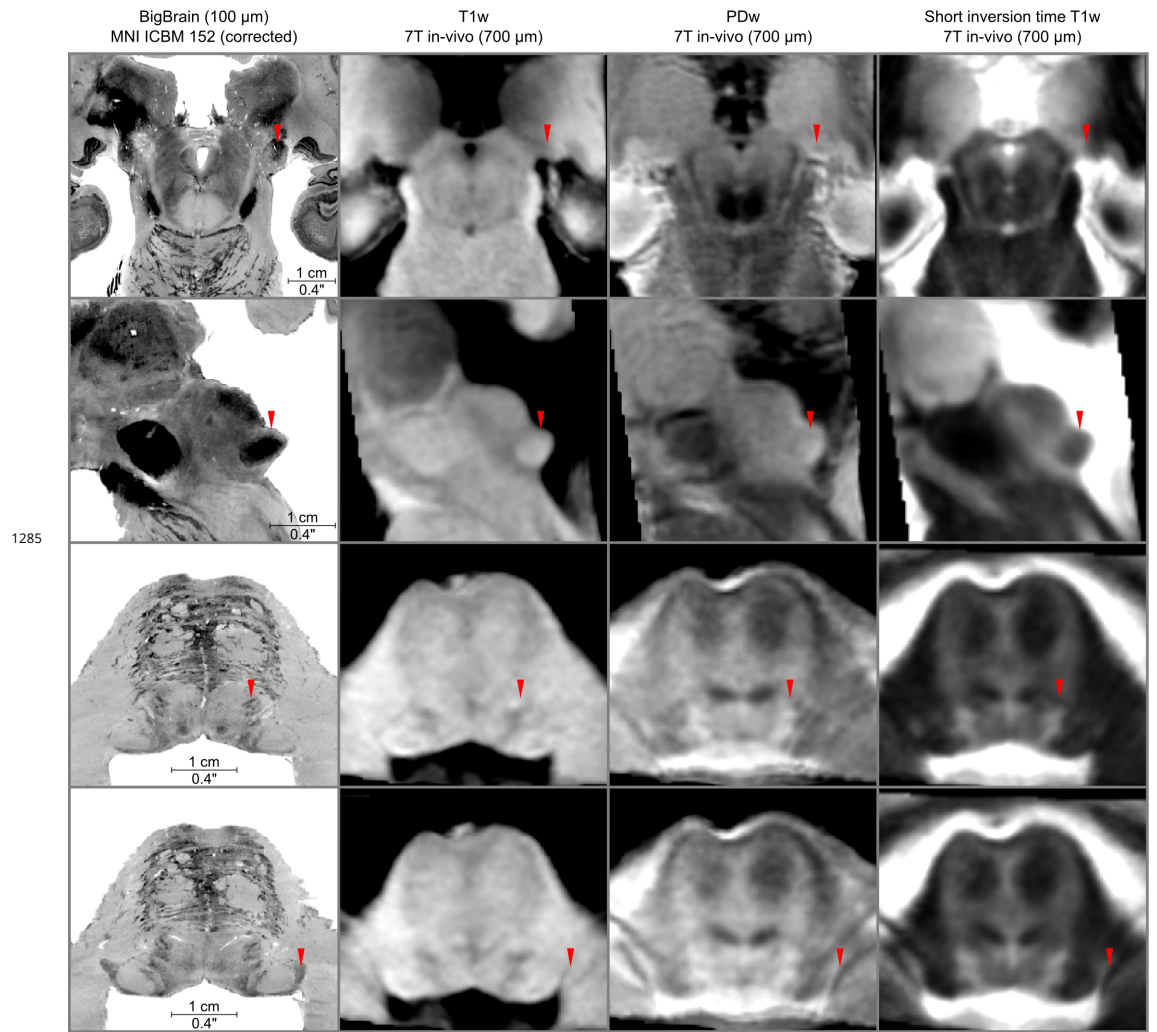


Figure 5–Figure supplement 1. In vivo anatomical group average images in MNI space.

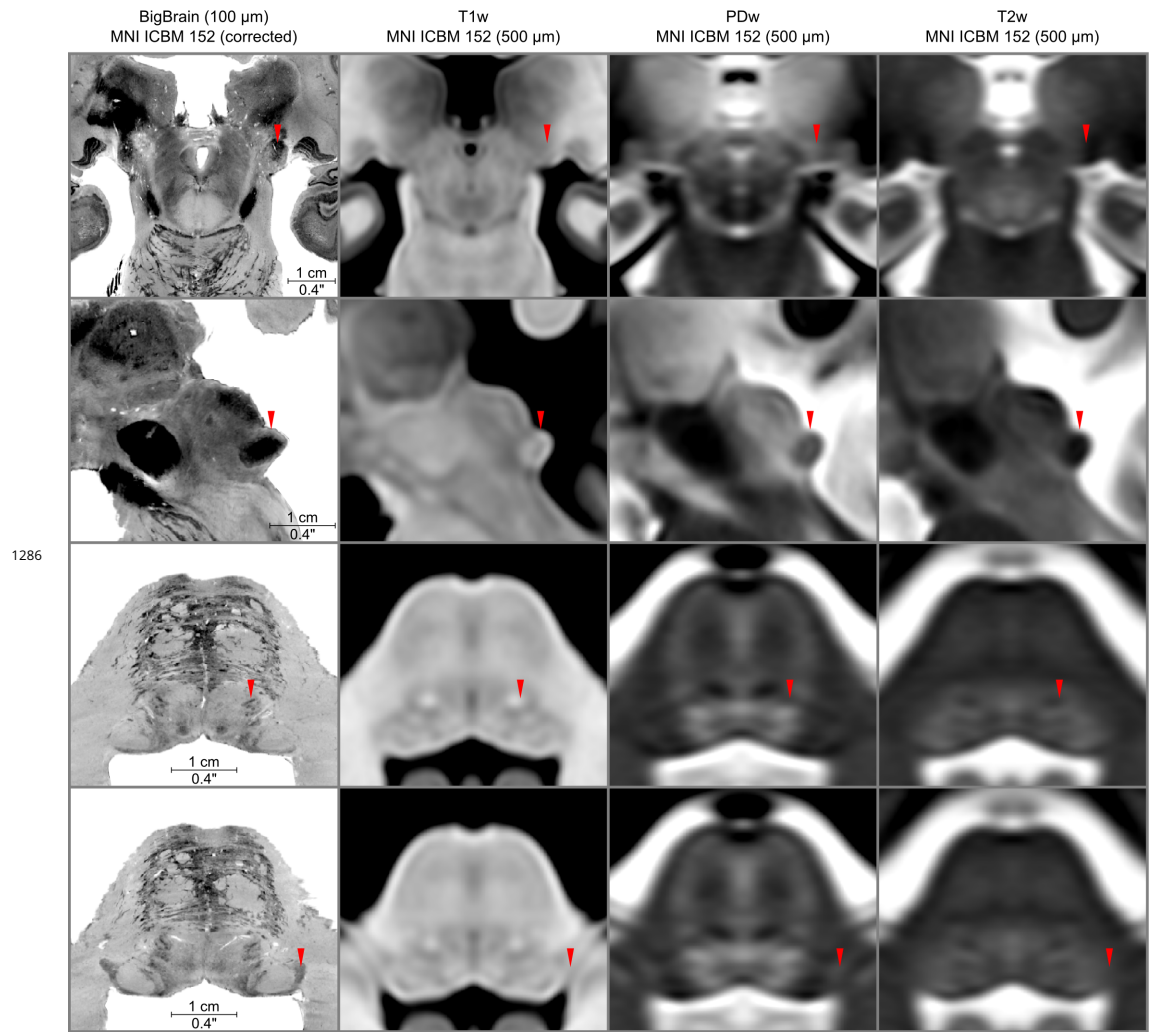


Figure 5-Figure supplement 2. Anatomical images from MNI ICBM 152 2009b dataset compared to BigBrain histology in MNIspace (left column).

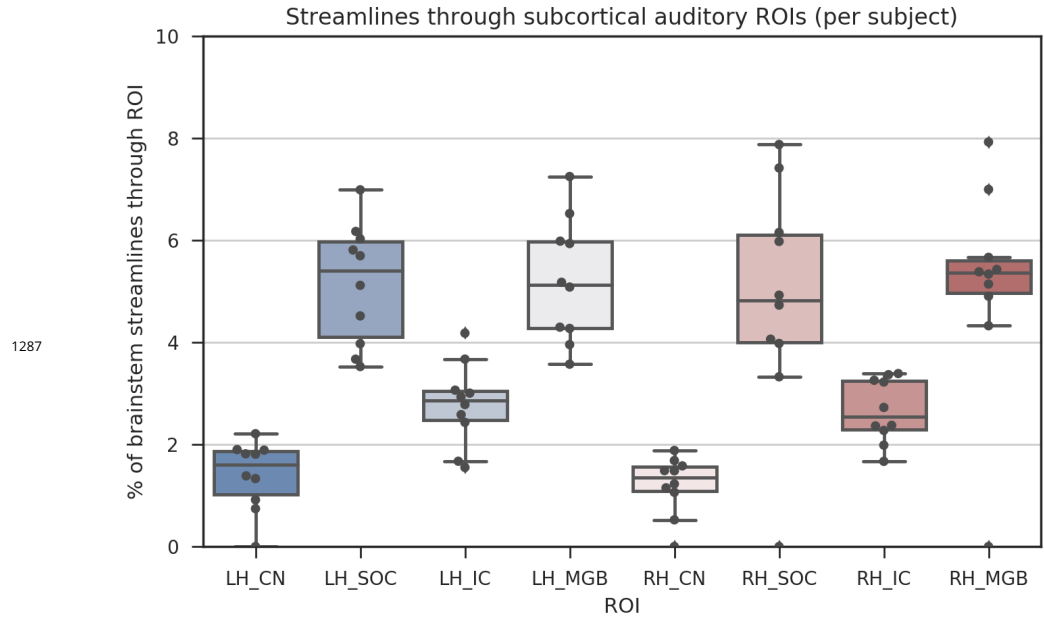


Figure 6-Figure supplement 1. Diffusion-weighted MRI tractography streamlines passing through each subcortical auditory region of interest for the ten in vivo participants. Bars represent 95% confidence intervals.